A NUCLEAR MAGNETIC RESONANCE PROBE OF GROUP IV CLATHRATES

A Dissertation

by

WEIPING GOU

Submitted to the Office of Graduate Studies of
Texas A&M University
in partial fulfillment of the requirements for the degree of

DOCTOR OF PHILOSOPHY

August 2008

Major Subject: Physics

A NUCLEAR MAGNETIC RESONANCE PROBE OF GROUP IV CLATHRATES

A Dissertation

by

WEIPING GOU

Submitted to the Office of Graduate Studies of
Texas A&M University
in partial fulfillment of the requirements for the degree of

DOCTOR OF PHILOSOPHY

Approved by:

Chair of Committee,	Joseph H. Ross, Jr.
Committee Members,	Donald G. Naugle
	Winfried Teizer
	Xinghang Zhang
Head of Department,	Edward S. Fry

August 2008

Major Subject: Physics

ABSTRACT

A Nuclear Magnetic Resonance Probe
of Group IV Clathrates. (August 2008)
Weiping Gou, B.S., Lanzhou University, China;
M.S., Academy of Science of China;
M.S., Texas A&M University
Chair of Advisory Committee: Dr. Joseph H. Ross, Jr.

The clathrates feature large cages of silicon, germanium, or tin, with guest atoms in the cage centers. The group IV clathrates are interesting because of their thermoelectric efficiency, and their glasslike thermal conductivity at low temperatures. Clathrates show a variety of properties, and the motion of cage center atoms is not well understood.

In $Sr_8Ga_{16}Ge_{30}$, we found that the slow atomic motion in the order 10^{-5} s is present in this system, which is much slower than what would be expected for standard atomic dynamics. NMR studies of $Sr_8Ga_{16}Ge_{30}$ showed that Knight shift and T_1 results are consistent with low density metallic behavior. The lineshapes exhibit changes consistent with motional narrowing at low temperatures, and this indicates unusually slow hopping rates. To further investigate this behavior, we made a series of measurements using the Carr-Purcell-Meiboom-Gill NMR sequence. Fitting the results to a hopping model yielded an activation energy of 4.6 K. We can understand all of our observations in terms of non-resonant atomic tunneling between asymmetric sites within the cages, in the presence of disorder.

For $Ba_8Ga_{16}Ge_{30}$, the relaxation behavior (T_1) deviates from the Korringa relation, and the Knight shift and linewidth change with temperature. Those results

could be explained by carrier freezout, and the development of a dilute set of magnetic moments due to these localized carriers. For $Ba_8Ga_{16}Ge_{30}$ samples made from Ga flux, we observed different T_1 and Knight shift behavior as compared to n type material. This is due to the differences in carrier type among these different samples. The p type sample has a smaller Knight shift and a slower relaxation rate than n type samples made with the stoichiometric ratio, which is consistent with a change in orbital symmetry between the conduction and valence bands.

WDS study for $Ba_8Al_{10}Ge_{36}$ showed the existence of vacancies in the Al-deficient samples, which results in some degree of ordering of Al occupation on the framework sites. In Al NMR measurements on $Ba_8Al_xGe_{40-x}$ with $x = 12$ to 16, we found that T_1 of all Al samples follows the Korringa relation. The broadening of the single NMR central peak of $Ba_8Al_{16}Ge_{30}$ is due to the inhomogeneous Knight shifts for occupation of different framework sites. For $Ba_8Al_{12}Ge_{34}$ and $Ba_8Al_{13}Ge_{33}$, we observed two peaks, and NMR results show that they are from distinct Al sites, while for each peak, the inhomogeneous broadening is much smaller. The difference in lineshapes we attributed to the existence of vacancies which we detected in the Al-deficient materials, and we assign one of the two Al peaks to Al adjacent to a vacancy.

ACKNOWLEDGMENTS

I would like to express my gratitude to my research advisor, Prof. Joseph H. Ross. I enjoyed fruitful discussions with him over these years, and appreciate very much his patience and expertise. I would not have accomplished this without him. I would like to thank Yang Li, Ji Chi and Venkat Goruganti for their daily suggestions and discussions on many issues. Many thanks go to Dr. Naugle and Dr. Rathnayaka for allowing me to use Arc melting instrument and helping me to measure transport and heat capacity of this study. I would also like to thank the committee members for their effort with my defense.

I owe special gratitude to my wife, Nan Wang for her understanding, inspiration, and all that she has done for me over these years. Finally I would like to acknowledge the Robert A. Welch Foundation and the Physics Department for the financial support during my Ph.D study.

TABLE OF CONTENTS

CHAPTER Page

LIST OF TABLES

LIST OF FIGURES

FIGURE Page

FIGURE Page

FIGURE Page

CHAPTER I

INTRODUCTION

A. Background

Clathrate, which comes from a Greek word meaning "locked", is defined in the Merriam-Webster dictionary as "relating to or being a compound formed by the inclusion of molecules of one kind in cavities of the crystal lattice of another". In 1811 Humphrey Davy gave the first evidence of a compound of water and chlorine gas which is now commonly known as a hydrate clathrate. Hydrate clathrates are a class of solids in which gas molecules occupy "cages" made up of hydrogen-bonded water molecules. Normally these "cages" are unstable when empty, collapsing into the conventional ice crystal structure, but they are stabilized by the inclusion of the gas molecule inside of them. Most low molecular weight gases such as H_2, O_2, CO_2, and CH_4, will form a hydrate under some pressure-temperature conditions [1, 2]. Hydrate clathrates are promising candidates for energy storage applications. The amount of methane potentially trapped in natural methane hydrate deposits may be significant, which makes them of major interest as a potential energy resource for the future.

Group IV elements such as silicon, germanium and tin can also form the same cage structures as hydrate clathrates. In general the term "clathrates" now refers to these open framework structure materials containing guest atoms inside the cages and atoms such as silicon, germanium, or tin in a crystalline framework of the cages. The cage center atoms are normally alkali metal, alkali earth or rare earth elements.

The journal model is *IEEE Transactions on Automatic Control*.

B. Structure of Some Clathrates

There are many types of group IV clathrates [3], and in this study we are interested in type-I and type-VIII. Type I clathrate, such as Ba/$Sr_8Ga_{16}Ge_{30}$ and β-$Eu_8Ga_{16}Ge_{30}$ [4], has the general formula A_8T_{46} (A = guest atom; T = Si, Ge, and Sn, plus group III or other framework elements) and is built up by 2 smaller T_{20} (dodecahedra) and 6 larger T_{24} (tetrakaidecahedra) polyhedra per cell. This structure contains three framework sites, $6c$, $16i$ and $24k$ in Wyckoff notation, and belongs to space group $Pm\bar{3}n$, No.223 as shown in Fig. 1 and Fig. 2(b).

Type VIII clathrate, such as $Ba_8Ga_{16}Sn_{30}$, and α-$Eu_8Ga_{16}Ge_{30}$ [4], has the same general formula as type I, but is built up by 20-hedral cages, formed by three 5-rings, three 6-rings and three 7-rings. This structure contains four framework sites, $8c$, $12d$, $2a$ and $24g$ in Wyckoff notation, and belongs to space group $I\bar{4}3m$, No.217 as shown in Fig. 2(a) and Fig. 3.

C. Various Properties of Group IV Clathrates

Clathrates are cage structure materials, and the cage center atoms are loosely bonded, in some versions known as "rattler" atoms, which make the clathrates very special. Si, Ge and Sn clathrates with Sr, Ba, Eu or alkali earth as guest atoms exhibit a variety of properties.

One of the most important properties is poor thermal conductivity and relatively high electric conductivity due to their special cage structure [5, 6, 7, 8, 9, 10, 11], which makes these clathrates good candidate for thermoelectric applications. Those clathrates often exhibit heavily doped semiconductor properties. At room temperature, resistivity is roughly $800\mu\Omega\cdot$cm and $600\mu\Omega\cdot$cm for typical $Ba_8Ga_{16}Ge_{30}$ and $Sr_8Ga_{16}Ge_{30}$ respectively [5]. At room temperature the thermal conductivity is about

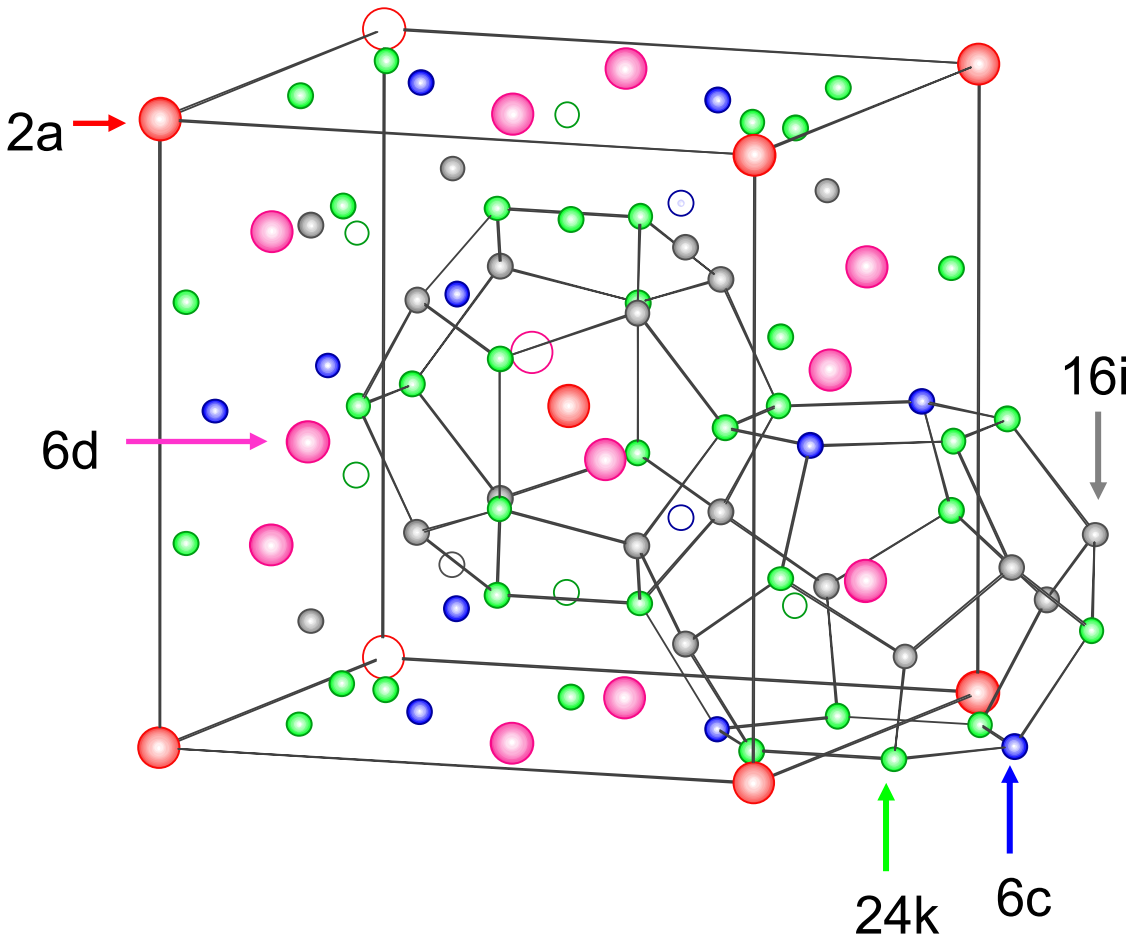

Fig. 1. Crystal structure of type-I clathrate

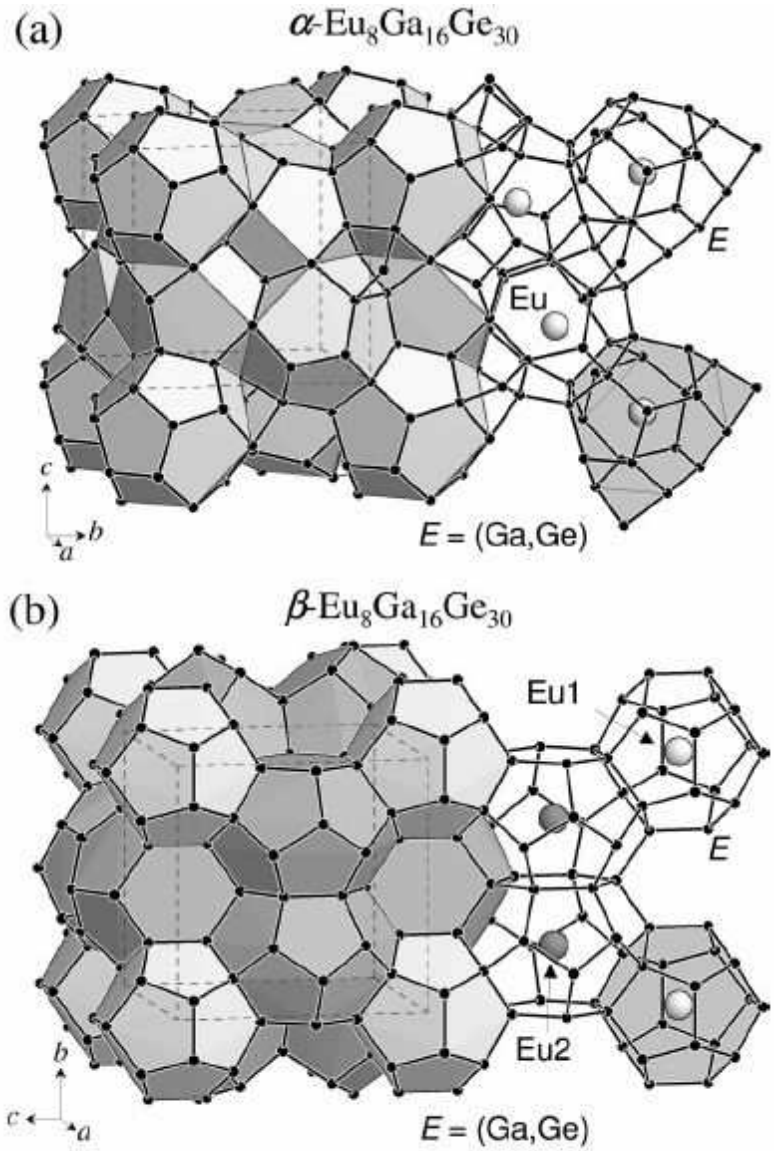

Fig. 2. (a) Crystal structure of type-VIII (α-$Eu_8Ga_{16}Ge_{30}$) clathrate; (b) Crystal structure of type-I (β-$Eu_8Ga_{16}Ge_{30}$) clathrate. (Eu is the cage center atom. Ge and Ga are the framework atoms) (Figure from ref. [4])

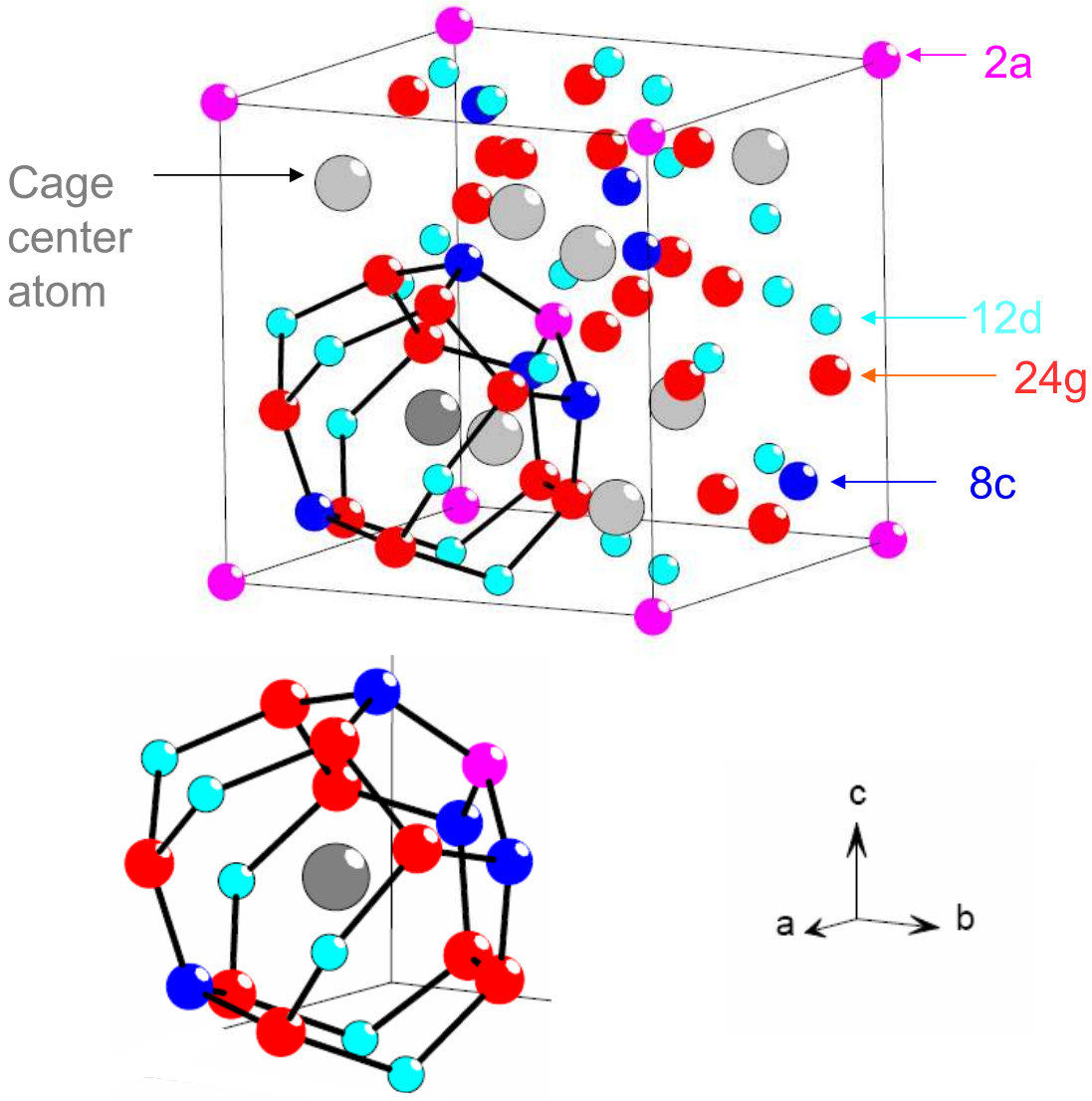

Fig. 3. Crystal structure of type-VIII clathrate and the structure of a single cage (at the bottom)

1.3 W/(m·K) for $Ba_8Ga_{16}Ge_{30}$ which is about the same as the room temperature value for vitreous silica [5].

Ferromagnetism was observed in $Eu_8Ga_{16}Ge_{30}$ clathrate. There exist two phases for $Eu_8Ga_{16}Ge_{30}$, the type-I structure known as β phase and the type-VIII structure known as α phase. T_C is found to be 10.5 K for α-$Eu_8Ga_{16}Ge_{30}$ and 36 K for β-$Eu_8Ga_{16}Ge_{30}$ [4]. Studies on $Ba_8Mn_xGe_{46-x}$ show that the structure is not stable with $x > 2$, and the spontaneous magnetization is approximately linearly proportional to the amount of Mn introduced and is maximized at $x = 2$ with T_C around 10 K [12]. Magnetization measurements also showed a large diamagnetic response in the $Ba_8Ge_{40}Cu_6$ clathrate [13].

A large magnetocaloric effect was observed in $Eu_8Ga_{16}Ge_{30}$ clathrates. Large entropy changes of 6 and 9.3 J /kg K were observed for the type-I and type-VIII phases, respectively [14].

Superconductivity was observed in Ba_8Si_{46} with $T_C = 8$ K due to strong sp^3 hybridization of s-electrons of Ba with the Si_{46} conduction-band states [15, 16]. The superconducting critical temperature in $Ba_8Si_{46-x}(Cu/Ga)_x$ is shown to decrease strongly with Cu and Ga content increasing [17, 18].

Density of states (DOS) calculations [7] show that $Ba_8Ga_{16}Ge_{30}$, $Sr_8Ga_{16}Ge_{30}$ and $Eu_8Ga_{16}Ge_{30}$ are semiconductors with a small band gap around 0.7 eV, and the Ba clathrate has a slightly larger band gap than Eu and Sr clathrates.

Specific heat measurements indicate an Einstein contribution from each of the rattler atoms, with a characteristic temperature of 60, 53, and 30 K for Ba, Sr, and Eu atoms respectively for type-I Ga-Ge clathrates [5].

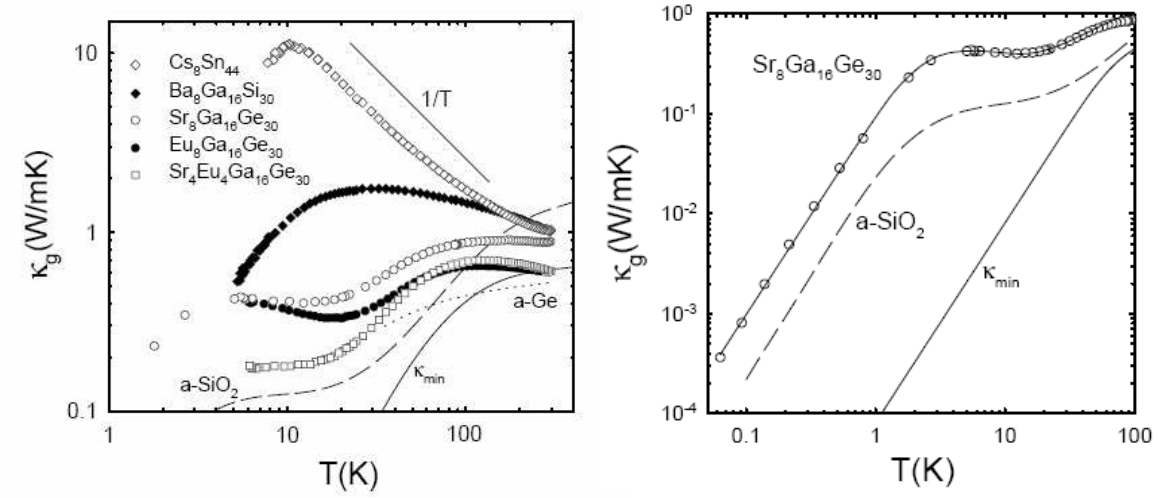

Fig. 4. Lattice thermal conductivity vs. temperature for the five clathrate specimens. The dashed and dotted curves are for a-SiO_2 and a-Ge, and the solid curve is the calculated minimum thermal conductivity of Ge [19]

D. Present Problems of Type-I Ga-Ge Base Clathrates

Although $Ba_8Ga_{16}Ge_{30}$, $Sr_8Ga_{16}Ge_{30}$ and $Eu_8Ga_{16}Ge_{30}$ have the same structure and behave similar in many ways, there are some key differences among them. One of the novel characteristics of the Eu and Sr clathrates is their very low, glasslike thermal conductivity. Although *n*-type Ba clathrate also exhibits very low thermal conductivity, it does not have a glasslike behavior, instead it has a behavior similar to a normal metal Fig. 4 [19, 5]. Single-crystal neutron-diffraction data (Fig. 5) show that Sr and Eu atoms in the larger cages of the type-I structure can move off the center position to one of four crystallographically equivalent positions, while Ba atoms can only stay at the cage center [5, 6]. This provides a connection between the thermal response and atomic displacement within the cages.

Low temperature ultrasonic attenuation measurements on a $Sr_8Ga_{16}Ge_{30}$ single crystal [20] provided direct evidence of a relatively high concentration of tunneling

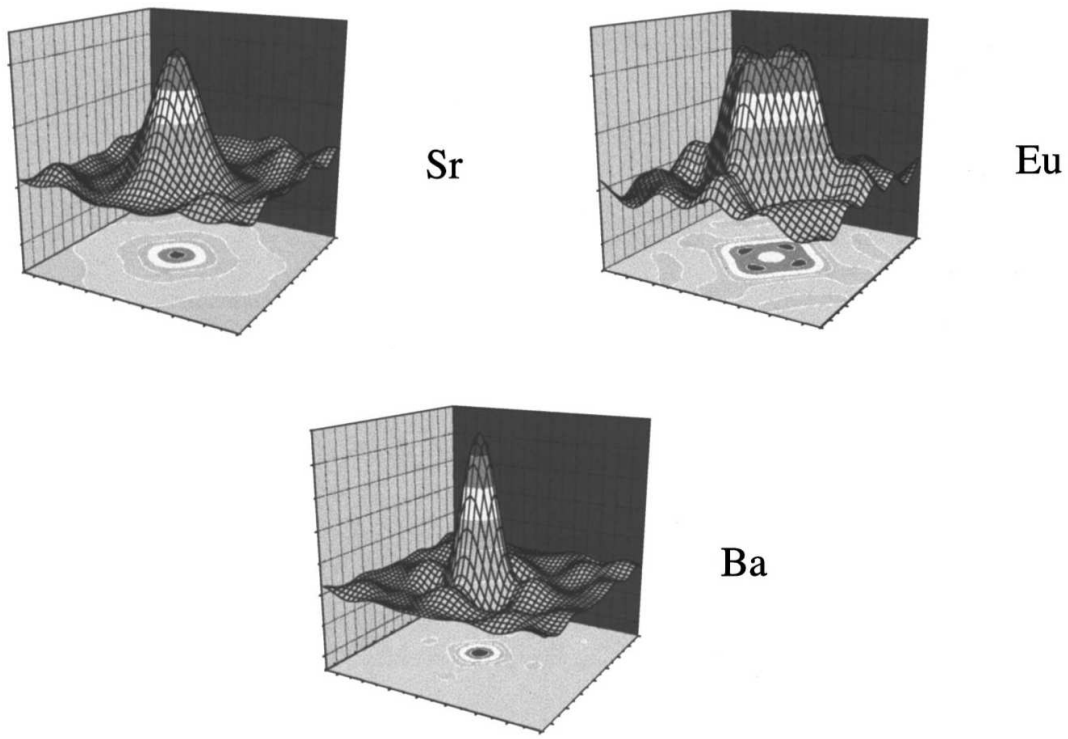

Fig. 5. Nuclear density at large-cage Ba, Sr, and Eu sites for $Ba_8Ga_{16}Ge_{30}$ and $Sr_8Ga_{16}Ge_{30}$ (15 K) and $Eu_8Ga_{16}Ge_{30}$ (40 K) from neutron-diffraction data [5]

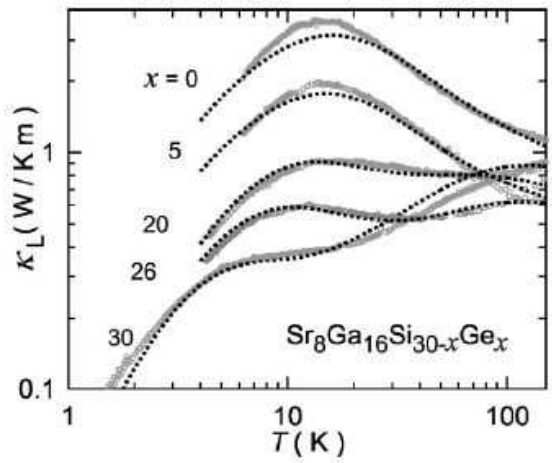

Fig. 6. Temperature dependence of lattice thermal conductivity for $Sr_8Ga_{16}Si_{30-x}Ge_x$ [22]

states, a feature normally associated with bulk glasses like SiO_2. A paper by Zerec *et al.* [21] posed a specific model for tunnel barriers between four-well tunneling states for Eu clathrate, and proposed that the resonant ultrasound behavior of Sr clathrate corresponds to transitions between quantized Einstein modes of Sr atoms in the cages. The Einstein temperature has been measured to be about 50 K in Sr clathrate [5]. However the thermal behavior observed at much low temperatures indicates that a set of disordered oscillator states with smaller barrier heights must also be important.

The relative cage size seems to play an important role for understanding the thermal conductivity. By growing homogeneous single crystals of $Sr_8Ga_{16}Si_{30-x}Ge_x$ in the full range of $0<x<30$, systematic control of cage size without changing the guest ion or the charge carrier type was achieved [22]. The lattice parameter expands by up to 3% with increasing Ge content, and as a consequence the free space for guest excursion increases in the cage. As a result, the lattice thermal conductivity in the low-temperature range from 10 K to 20 K is suppressed in such a way that

the crystallinelike peak found for $Sr_8Ga_{16}Si_{30}$ evolves into the well-known glasslike behavior of $Sr_8Ga_{16}Ge_{30}$ (see Fig. 6). Studies on the substitution of In atoms for Ga atoms in $Ba_8Ga_{16}Ge_{30}$ show that it leads to a decrease in thermal conductivity [23]. Because a In atom has larger atomic radius than a Ga atom, the substitution of In atoms for Ga atoms will result in a larger cage size.

However, thermal conductivity measurements [8, 24] on p-type $Ba_8Ga_{16}Ge_{30}$ gave results which are similar to $Sr_8Ga_{16}Ge_{30}$ and have a dip/plateau region near 15 K and T^2 behavior at very low T (see Fig. 7). According to various recent experiments, in addition to the guest atom tunneling explanation [21, 19], researchers have proposed several alternative explanations for the low T temperature dependence of the lattice thermal conductivity in the clathrates, such as phonon charge-carrier scattering [8, 25], off-center rattler-phonon scattering [26, 27], a soft potential model based on tunneling of two level system [24], and the interaction and hybridization of the low-energy rattling modes with the propagating acoustic modes of the framework [28]. The research community has not reached an agreement on this matter.

The carrier type (n- or p-type) and its concentration depend on the deviation from the ideal stoichiometry. To my knowledge, all samples of $Sr_8Ga_{16}Ge_{30}$ and $Eu_8Ga_{16}Ge_{30}$ reported so far are of the n-type, while $Ba_8Ga_{16}Ge_{30}$ can be p-type or n-type metallic depending the sample preparation process [8, 29, 24, 30], and can exhibit metal or semiconductor electronic properties. That is one of the reasons why so many properties are sample dependent. Carrier localization and delocalization was proposed for Na-Si clathrate to explain temperature dependent Knight Shift data measured by NMR [31], and carrier localization will have a big impact on the electronic properties. The defects responsible for this behavior are poorly understood.

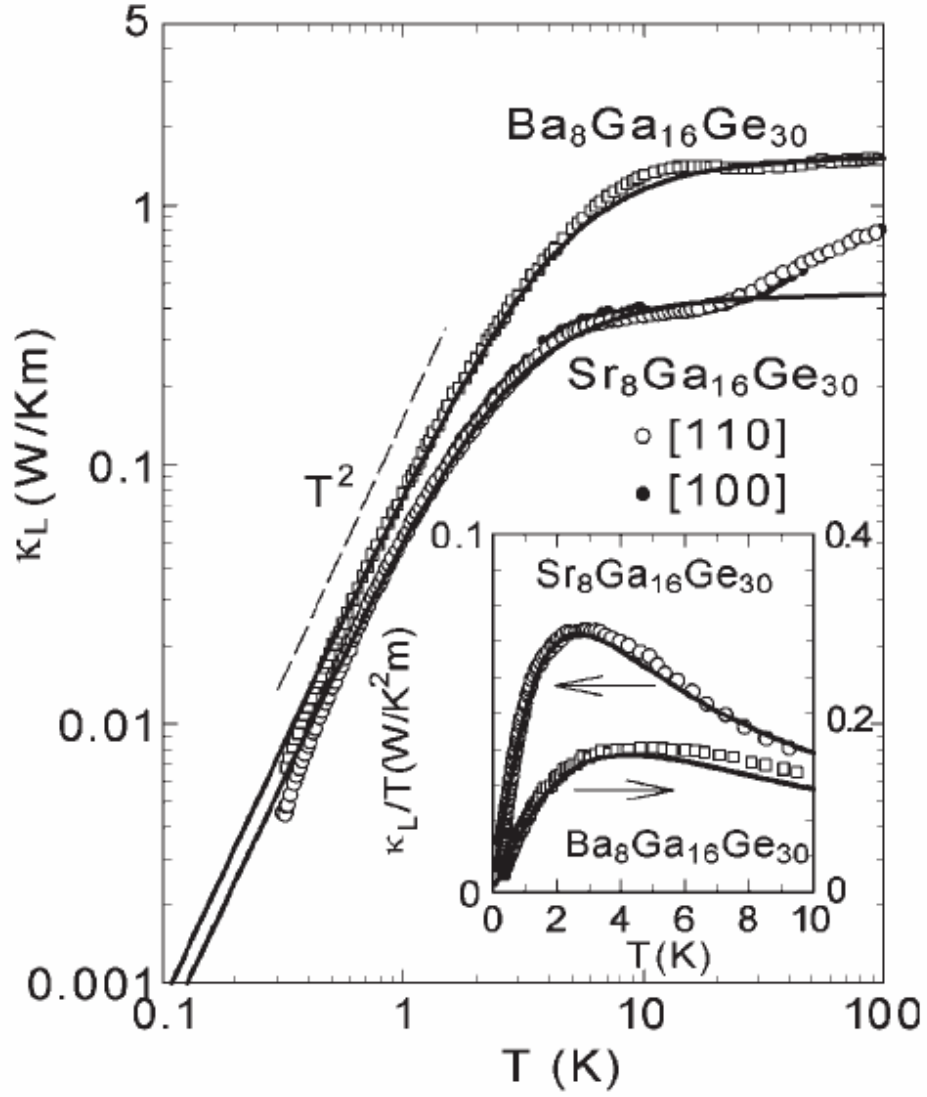

Fig. 7. Temperature dependence of lattice thermal conductivity for single-crystalline p-type $Ba_8Ga_{16}Ge_{30}$ and n-type $Sr_8Ga_{16}Ge_{30}$ [24]

E. Purpose of This Study

To understand the motion of cage center atoms, and investigate the electronic and magnetic properties among clathrates, we applied the nuclear magnetic resonance (NMR) technique. NMR is a local probe, which can tell us local electronic and magnetic information. The long coherence times allow NMR to be used to study relatively low-frequency atomic dynamics.

CHAPTER II

INTRODUCTION TO SOLID STATE NMR

Nuclear Magnetic Resonance, or NMR as it is usually called, was developed in its present form in 1945 by the physicists Bloch and Purcell. In this chapter, I briefly review the basic concepts of NMR related to the electronic and magnetic properties in solids. Thorough discussions are covered in textbooks by Slichter [32] and Abragam [33].

A. Basic Theory

The idea of NMR is not very complicated. A nucleus may consist of many particles coupled together so that in any given state, the nucleus possesses a total magnetic moment $\vec{\mu}$ and angular momentum $\hbar\vec{I}$. We can write

$$\vec{\mu} = \gamma_n \hbar \vec{I}, \tag{2.1}$$

where γ_n is called the nuclear gyromagnetic ratio, which is different for different types of nuclei. Because of its having magnetic moment, the nucleus will interact with an external magnetic field. The interaction energy between a nucleus and a magnetic field $\vec{H}$ is -$\vec{\mu}$·$\vec{H}$. Then we have a simple Hamiltonian:

$$\mathcal{H} = -\vec{\mu} \cdot \vec{H}. \tag{2.2}$$

Taking the field to be H_0 along the z-direction, then

$$\mathcal{H} = -\gamma_n \hbar H_0 I_z. \tag{2.3}$$

The eigenvalues of this Hamiltonian are simply multiples of the eigenvalues of I_z, and the allowed values are

$$E = -m\gamma_n \hbar H_0, m = I, I-1, ..., -I. \tag{2.4}$$

To detect the presence of such a set of energy levels, one can apply RF to the system to see the spectral absorption. To make the transition happen, the frequency ω_0 of RF must satisfy

$$\hbar\omega_0 = \Delta E = \gamma_n \hbar H_0, \tag{2.5}$$

where ΔE, the energy difference between two adjacent levels, is called the Zeeman energy, and ω_0 is called the Larmor frequency. When an RF field with frequency ω_0 is applied to the sample, it will cause transitions between neighboring states with the selection rule $\Delta m = \pm 1$, or in other words, it gives rise to the nuclear magnetic resonance.

However, in reality, the magnetic field seen by a nucleus may not simply be the external field H_0 applied. Interactions such as the dipole-dipole interaction and the interaction between the electron and nucleus will modify the magnetic field seen by a nucleus. In the end of this chapter, we will discuss the situation of interactions between the free electron and nucleus.

B. Line Shape

Normally the NMR spectrum of a sample is not simply a narrow line with frequency ω_0. It has a certain shape due to the fact that different nuclei of the sample may feel different magnetic fields, and the resonance frequency of an individual nucleus is decided by the total magnetic field seen by that nucleus. The NMR line shape depends on several different factors. Because of the inhomogeneity of the applied magnetic field, there will be a spread of the Larmor frequencies, resulting in the broadening of the lineshape. For a nucleus of $I > 1/2$ in a non-cubic environment,

quadrupole effects can also broaden the lineshape. We will discuss this in the next section. The dipole-dipole interaction between two nuclear spins is one of the most common factors to cause the broadening of a line shape, and obscure the true NMR pattern. The presence of magnetic impurities in diluted crystals will also cause the NMR line broadening via dipolar couplings.

C. Electric Quadrupole Effects

Quadrupole effects in the NMR lines are caused by the interaction of the nuclear quadrupole moment Q, with the electric field gradient (EFG) experienced by the nucleus. For $I \leq \frac{1}{2}$ the average quadrupole interaction is zero in any crystallographic environment so that no quadrupole effects are seen in the NMR spectra. Quadrupole effects can only be seen for nuclei with $I > \frac{1}{2}$, where the electric field gradient seen by the nucleus varies with orientation. The resulting lineshapes depend upon the relative strength of the magnetic and quadrupole fields [32, 34]. In high magnetic field, it can be shown that the first order quadrupole effect does not shift the central line ($\frac{1}{2} \leftrightarrow$ -$\frac{1}{2}$), but it will shift the frequency of other transitions. The second order quadrupole effect will cause a shift and the splitting of all transitions. The shift of the central line due to the second order quadrupole coupling is in the order of $(e^2qQ)^2/\gamma_n\hbar H_0$ [32], where $eq = \frac{\partial^2 V}{\partial z^2}$, the z component of the field gradient, which changes with orientation in the filed. Thus quadrupole effects will cause the broadening the lineshape.

D. Relaxation Time

At equilibrium, the distribution of nuclei among the energy levels is given by the Boltzmann distribution. When RF is applied to the nuclear system, the equilibrium is disrupted, and the nuclear spin system has the tendency to return to equilibrium,

or in other words to relax. When a relaxation process involves the energy change between nuclear spin and the surroundings (the "lattice"), it is called spin-lattice relaxation, and characterized by a time T_1, the spin-lattice relaxation time. During the relaxation process, nuclear spins with the same energy can exchange orientations, and this process does not involve the energy, it is called spin-spin relaxation, and characterized by a time T_2, the spin-spin relaxation time.

E. Nuclei in a Metal

Most of our samples show metallic behavior. In this section, we will discuss some NMR results related to such situations where we consider the interactions of nuclei with free electrons.

1. Knight Shift

The Hamiltonian of the interaction of a nucleus with a free electron can be written as:

$$\mathcal{H} = -\frac{8\pi}{3}\vec{\mu_e}\cdot\vec{\mu_n}\delta(r) + [\frac{\vec{\mu_e}\cdot\vec{\mu_n}}{r^3} - \frac{3(\vec{\mu_e}\cdot\vec{r})(\vec{\mu_n}\cdot\vec{r})}{r^5}] - \frac{e}{m}\frac{\vec{l}\cdot\vec{\mu_n}}{r^3}, \tag{2.6}$$

where $\vec{r}$ is the radius vector of the electron with the nucleus at the origin, $\vec{\mu_e}$ is the electron spin moment, $\vec{\mu_n}$ is the nuclear moment, and $\vec{l}$ is the orbital angular momentum of the electron. In this formula, the first term is the Fermi contact interaction term, which is non-zero only for s electrons. The next two terms describe the magnetic dipole interaction between the electron and nucleus. The last term is the interaction of angular momentum with the nucleus. When we average $\mathcal{H}$ over an s-state electron wave function, the second and third terms will vanish in Eqn. 2.6 due to the spherical symmetry of the s-state wave function, and only the first term survives. Assuming the applied field is along the z-axis, the effective Fermi contact

interaction can be written as [32]

$$\mathcal{H} = -\gamma_n \hbar I_Z [\frac{8\pi}{3} \langle |\Psi_s(0)|^2 \rangle_{E_F} \chi_P H_0], \tag{2.7}$$

where χ_P is the Pauli paramagnetic spin susceptibility, and $\langle |\psi_s(0)|^2 \rangle_{E_F}$ relates to the average over electrons at Fermi level.

The small energy in Eqn. 2.7 is entirely equivalent to the interaction with an *extra* magnetic field ΔH, which aids the applied the applied field H_0. It will cause a resonance frequency shift, called the Knight Shift, and defined as

$$K = \frac{\Delta H}{H_0} = \frac{8\pi}{3} \langle |\Psi_s(0)|^2 \rangle_{E_F} \chi_P. \tag{2.8}$$

From this formula, we can conclude certain properties of Knight Shift. First, it is alway positive. Second, it is independent of the applied field. Finally, as long as both $\langle |\psi_s(0)|^2 \rangle_{E_F}$ and χ_P are independent of the temperature, K is as well.

The interaction of an electron with the nucleus is also called hyperfine coupling, and the hyperfine field is defined as

$$H_{hf} = \mu_B \frac{8\pi}{3} \langle |\Psi_s(0)|^2 \rangle_{E_F}. \tag{2.9}$$

Therefore, the Knight Shift due to the Pauli susceptibility in Eqn. 2.8, denoted as K_s, can be written as

$$K_s = \frac{H_{hf}}{\mu_B} \chi_P. \tag{2.10}$$

From the free electron model, the Pauli susceptibility χ_P can be found as

$$\chi_P = \mu_B^2 g(E_F), \tag{2.11}$$

where $g(E_F)$ is the electronic DOS at the Fermi surface. Thus if the hyperfine field is known, the Knight shift can be used to determine $g(E_F)$.

Besides the contribution to the Knight Shift from the contact interaction as we have discussed earlier, there are several other sources of contribution to the Knight Shift, such as core polarization, and orbital interaction. Normally the contact interaction contribution dominates [34].

2. Korringa Relation

In a metal, the relaxation of nuclei is mainly due to the interaction of nuclear spins with conduction electrons. Such an interaction is a sum over all electron states able to participate in the relaxation process, and only electrons at Fermi level can participate in the relaxation process. For a paramagnetic metal, the Fermi contact interaction is usually dominant, and the corresponding T_1 is given by [32]

$$\frac{1}{T_1 T} = \frac{64}{9} k_B \pi^3 \hbar^3 \gamma_e^2 \gamma_n^2 [\langle |\Psi_s(0)|^2 \rangle_{E_F}]^2 g^2(E_F), \tag{2.12}$$

where γ_e is the electron gyromagnetic ratio. Combining Eqn. 2.8, Eqn. 2.11, and Eqn. 2.12, we can get

$$K^2 T_1 T = \frac{\hbar}{4\pi k_B} \frac{\gamma_e^2}{\gamma_n^2}, \tag{2.13}$$

where k_B is the Boltzmann constant. This result is called the Korringa relation. $K^2 T_1 T$ is called the Korringa product, and its enhancement is indicative of the strength of correlations [35, 36, 37, 38]. The Korringa relation tells that in a paramagnetic metal system, $T_1 T$ is independent of the temperature, which is an indication of metallic properties of the sample. The presence of the dilute magnetic moments, or a change of electronic structure with temperature could result in a deviation from the Korringa relation.

F. Relaxation in a Semiconductor

In a semiconductor, the relaxation rate may not obey the Korringa relation, because the carrier density can depend on the temperature, and the susceptibility may not follow the Pauli form. With an increase in the temperature for an intrinsic semiconductor, more and more electrons are activated into the conduction band according to an exponential function. It can be shown that in such a semiconductor T_1 follows the following relation [39]:

$$\frac{1}{T_1 T} = C T e^{-\Delta\epsilon/k_B T}, \tag{2.14}$$

where C is a constant depending on the effective mass, as well as other factors, k_B is the Boltzmann constant, and $\Delta\epsilon$ is the energy gap.

CHAPTER III

BASIC PRINCIPLES AND TECHNIQUES OF NMR

A. Equations of Motion

To clearly see how pulsed NMR works, we will look at how the nuclear magnetic moment responds to a static applied magnetic field and RF field.

In the equilibrium condition, a nuclear spin system will form a macroscopic magnetization $\vec{M}$ with a total angular momentum $\vec{L}$. The applied magnetic field, $\vec{H}$ will produce the torque $\vec{M} \times \vec{H}$ on $\vec{L}$, and force $\vec{M}$ to precess about $\vec{H}$. Thus the equation of the motion is

$$\frac{d\vec{M}}{dt} = \gamma_n(\vec{M} \times \vec{H}). \tag{3.1}$$

The frequency of $\vec{M}$ precessing about the field is $\gamma_n H_0$. Viewed from the laboratory frame with consideration of the relaxation, we have the Bloch equations [32]:

$$\frac{dM_x}{dt} = \gamma_n(\vec{M} \times \vec{H})_x - \frac{M_x}{T_2}, \tag{3.2}$$

$$\frac{dM_y}{dt} = \gamma_n(\vec{M} \times \vec{H})_y - M_y T_2, \tag{3.3}$$

$$\frac{dM_z}{dt} = \gamma_n(\vec{M} \times \vec{H})_z - \frac{M_z - M_0}{T_1}, \tag{3.4}$$

where M_0 is the equilibrium magnetization of a sample in an external field which we assume to be along the z-axis. T_1 is spin-lattice relaxation time, which takes place relative to the z-axis, and involves energy change. T_2 is the spin-spin relaxation time, which takes place relative to the x-y plane, and involves no energy change.

The pulsed NMR process is very clear and simple, if we look at the motion of magnetization in the frame rotating with respect to the laboratory frame. The total

time derivative of $\vec{M}$ and its partial time derivative can be related in this way:

$$(\frac{d\vec{M}}{dt})_{lab} = (\frac{\partial\vec{M}}{\partial t})_{rot} + \vec{\omega} \times \vec{M}. \tag{3.5}$$

where $\vec{\omega}$ is the rotating frequency of $\vec{M}$. Combining this with Eqn. 3.1, we obtain

$$(\frac{\partial\vec{M}}{\partial t})_{rot} = \gamma_n(\vec{M} \times \vec{H}) + \vec{M} \times \vec{\omega} = \gamma_n\vec{M} \times (\vec{H} + \frac{\vec{\omega}}{\gamma_n}) = \gamma_n(\vec{M} \times \vec{H_{eff}}), \tag{3.6}$$

where H_{eff}, with $\vec{H}_{eff} = \vec{H} + \frac{\vec{\omega}}{\gamma_n}$, is the effective magnetic field seen by the nuclear moment in the rotating frame of reference. If the rotating frame has an angular frequency equal to $-\gamma_n\vec{H}$, the effective field $\vec{H}_{eff}$ vanishes, and $\vec{M}$ is invariant with time in the rotating frame. If we apply an RF field with frequency ω to the coil which is perpendicular to the static field H_0, the RF will generate an H_1 field perpendicular to H_0, and H_1 will be static in the rotating reference frame if it is on resonance. Thus the effective field in the rotating frame shown in Fig. 8(a) can be written as

$$\vec{H}_{eff} = \vec{H}_0 + \frac{\vec{\omega}}{\gamma_n} + \vec{H}_1, \tag{3.7}$$

At resonance, ω/γ_n will cancel the external field and leaves only $\vec{H}_1$ in the x′-y′ plane shown in Fig. 8(b). Therefore the angular nutation frequency about $\vec{H}_1$ is $\gamma_n H_1$ and in a time period t, the angle θ through which $\vec{M}$ nutates is

$$\theta = \gamma_n H_1 t. \tag{3.8}$$

B. Pulse Sequences and Techniques

1. FID and Spin-Echo

In pulsed NMR experiments, an intense RF pulse in the laboratory frame is applied to the sample to excite the nuclei whose resonance frequency is close to the pulse frequency. Immediately following the pulse, the nuclear magnetic moment will relax

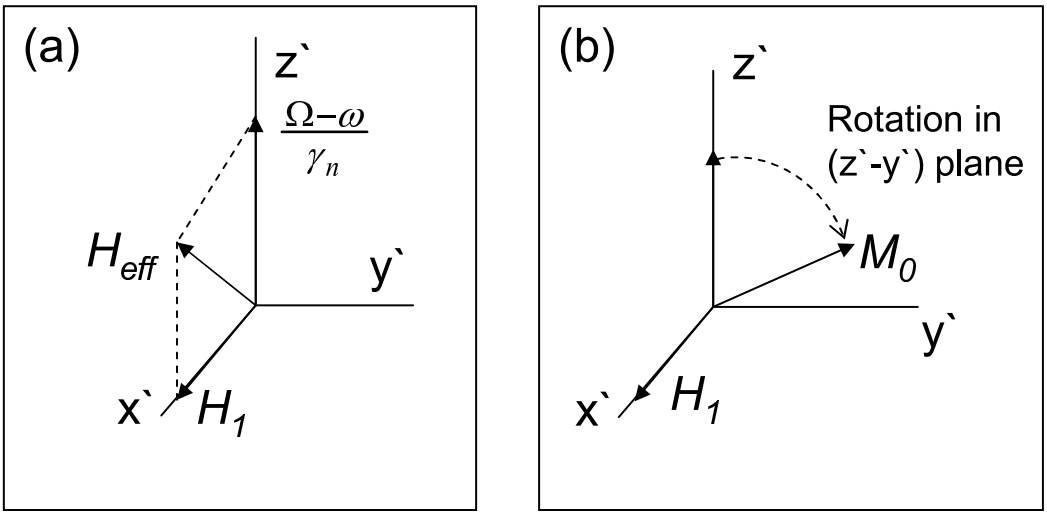

Fig. 8. (a)Effective field in rotating frame reference, where $\Omega = \gamma_n H$; (b) At resonance, H_{eff} is equal to H_1, and in x′-axis for this case, $\vec{M}$ precesses about x′-axis in (x′-z′) plane.

to its equilibrium condition, or in other words, decay, and this process called the free induction decay (FID) will induce a electric signal in the coil. The FID signal decays with the behavior described by Eqn. 3.2 and Eqn. 3.3. The inhomogeneity of the applied magnetic field can also causes nuclear spins in the x-y plane to defocus and make the FID signal decay. The decay time constant $T_2^\star$ can be found as

$$\frac{1}{T_2^\star} = \frac{1}{T_2} + \gamma_n \Delta H_0, \tag{3.9}$$

where ΔH_0 is the width of the inhomogeneity of the applied magnetic field, and T_2 is the spin-spin relation time. By applying advanced pulse techniques, the defocusing of the spin due to inhomogeneity of the external field can be refocused [32].

Normally, if an RF pulse makes the magnetic moment $\vec{M}$ rotate 90° around the x′-axis in the rotating reference frame, the pulse is called a 90°_x pulse. After this 90°_x pulse, $\vec{M}$ will defocus in x′-y′ plane mainly due to the field inhomogeneity. In the rotating reference frame, nuclear spins with a large local field will rotate faster, and nuclear spins with a small local field will rotate more slowly. Thus we see the defocusing of the nuclear spins in the x′-y′ plane (see Fig. 9). If we apply a 180°_y pulse at time τ after 90°_x pulse, it will flip all nuclear spins by 180°_x around the y′-axis. After that, again the nuclear spins will undergo defocusing. Because the local field does not change, fast rotating spins remain fast and slow rotating spins remain slow. Therefore a spin echo will form exactly at time τ after 180°_y pulse (see Fig. 9). This pulse sequence is also called the Hahn spin-echo sequence, which is the most common method to observe a spin echo.

2. T_1 Measurement

If we first apply a 180° pulse to the sample in equilibrium, it will flip the magnetic moment, $\vec{M}$ to the -z direction. By observing how fast $\vec{M}$ recovers to the +z direction,

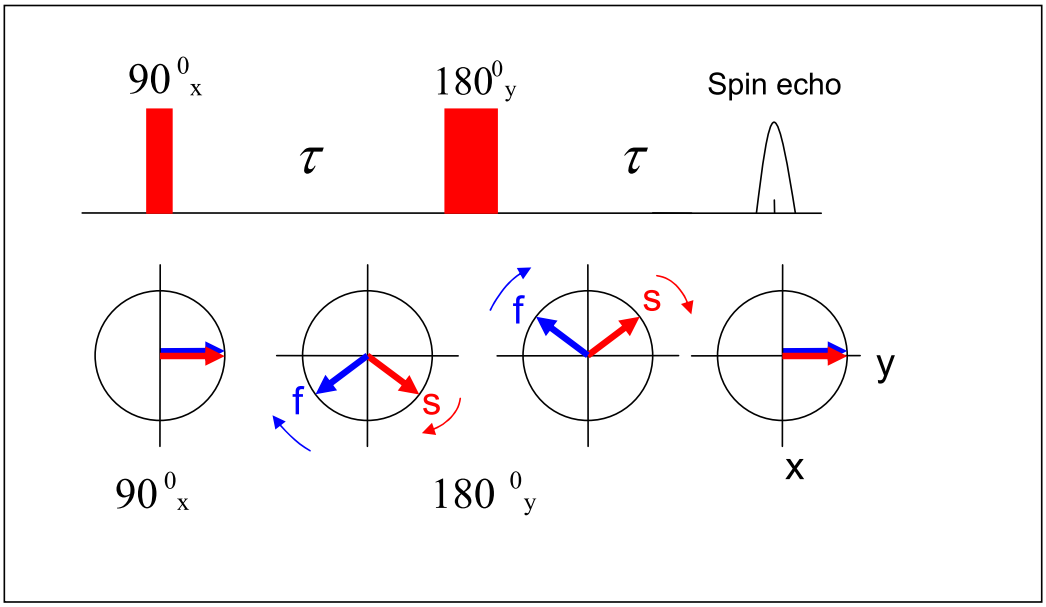

Fig. 9. Two pulse Hahn spin-echo sequence

we can calculate the spin-lattice relaxation time T_1. The sequence for T_1 measurement is 180° - T_{wait} - 90° - τ - 180°. The last two pulses are the same as Hahn spin-echo sequence. By measuring the intensity of the spin echo, we can know what M_z is at time T_{wait} after first 180° pulse. In the measurement, τ is fixed, and we vary T_{wait} to get a recovery curve. The formulas to describe the magnetization recovery curve are given in [40]. By fitting the recovery curve, we can obtain T_1. Depending on the size of the spin and transition measured, the expression will be different. For spin $\frac{3}{2}$, for example as in Ga nuclei, the recovery curve for the central transition ($\frac{1}{2} \leftrightarrow$ -$\frac{1}{2}$) is given as

$$\frac{M(t)}{M(0)} = 0.1e^{-\frac{\tau_{wait}}{T_1}} + 0.9e^{-\frac{6\tau_{wait}}{T_1}}. \tag{3.10}$$

For spin $\frac{5}{2}$ nuclei such as Al nuclei, the recovery curve for a central transition ($\frac{1}{2}$ $\leftrightarrow$ -$\frac{1}{2}$) is given as

$$\frac{M(t)}{M(0)} = 0.0286e^{-\frac{\tau_{wait}}{T_1}} + 0.178e^{-\frac{6\tau_{wait}}{T_1}} + 0.793e^{-\frac{15\tau_{wait}}{T_1}}. \tag{3.11}$$

3. CPMG Sequence

In spin echo measurement, we assume that the local field seen by each individual nuclear spin does not change before the formation of the echo. After a 180° pulse, fast-rotating spins remain fast, and slow-rotating spins remain slow. Therefore, spin defocusing due to inhomogeneity of applied field can be refocused. However, due to reasons such as atomic diffusion, atom jumping, or motion in liquids, the local field seen by each individual spin may change fter the 180° pulse of a spin-echo experiment. Due to these reasons spin defocusing due to these reasons can not be refocused by the spin-echo sequence.

Using a Carr-Purcell-Meiboom-Gill (CPMG) pulse sequence we can refocus some diffusing spins despite the change of local field. The CPMG sequence is 90_x-τ-[180_y-τ-(echo)-τ-]^n, whereτ is half of the spacing between 180° pulses (see Fig. 10(a)). For n cycles 2τ, we can observe a series of spin echos in a CPMG sequence, and the intensity of a spin echo formed at time $2n\tau$ is given as [32]

$$M(n2\tau) = M_0 exp[-(\gamma_n \frac{\partial H}{\partial z})^2 D(n2\tau)\frac{1}{3}\tau_2]exp(-n2\tau/T_2), \tag{3.12}$$

where D is the diffusion constant and $\frac{\partial H}{\partial z}$ is the gradient of the static field. The difference between spin echo and CPMG sequences is shown in Fig. 10(b). We can observe a spin echo at time T for both the Hahn echo and CPMG sequences. Because CPMG can refocus some spin-defocusing due to the change of the local field, while the spin-echo sequence does not, the amplitude of the spin echo observed by CPMG at time T is larger than the amplitude observed by the spin-echo sequence.

4. Magic Angle Spinning

Nuclear dipolar-dipolar coupling is orientation-dependent. It is proportional to $P_2(\cos\theta)$, where $P_2(\cos\theta) = (3\cos^2\theta\text{-}1)/2$. This term becomes zero when $(3\cos^2\theta\text{-}1)/2 = 0$, or $\theta \approx 54.74°$. This is the so-called magic angle. Spinning a sample rapidly at this angle with respect to the magnetic field can average the orientation dependence to zero. This is called the Magical Angle Spinning (MAS) technique. If the spinning rate is larger than the frequency range of the orientation dependent lineshape, a single narrow line will result. If the spinning rate is less than the width of the lineshape, only partial averaging occurs and a set of narrow spinning sidebands can show up as well [32].

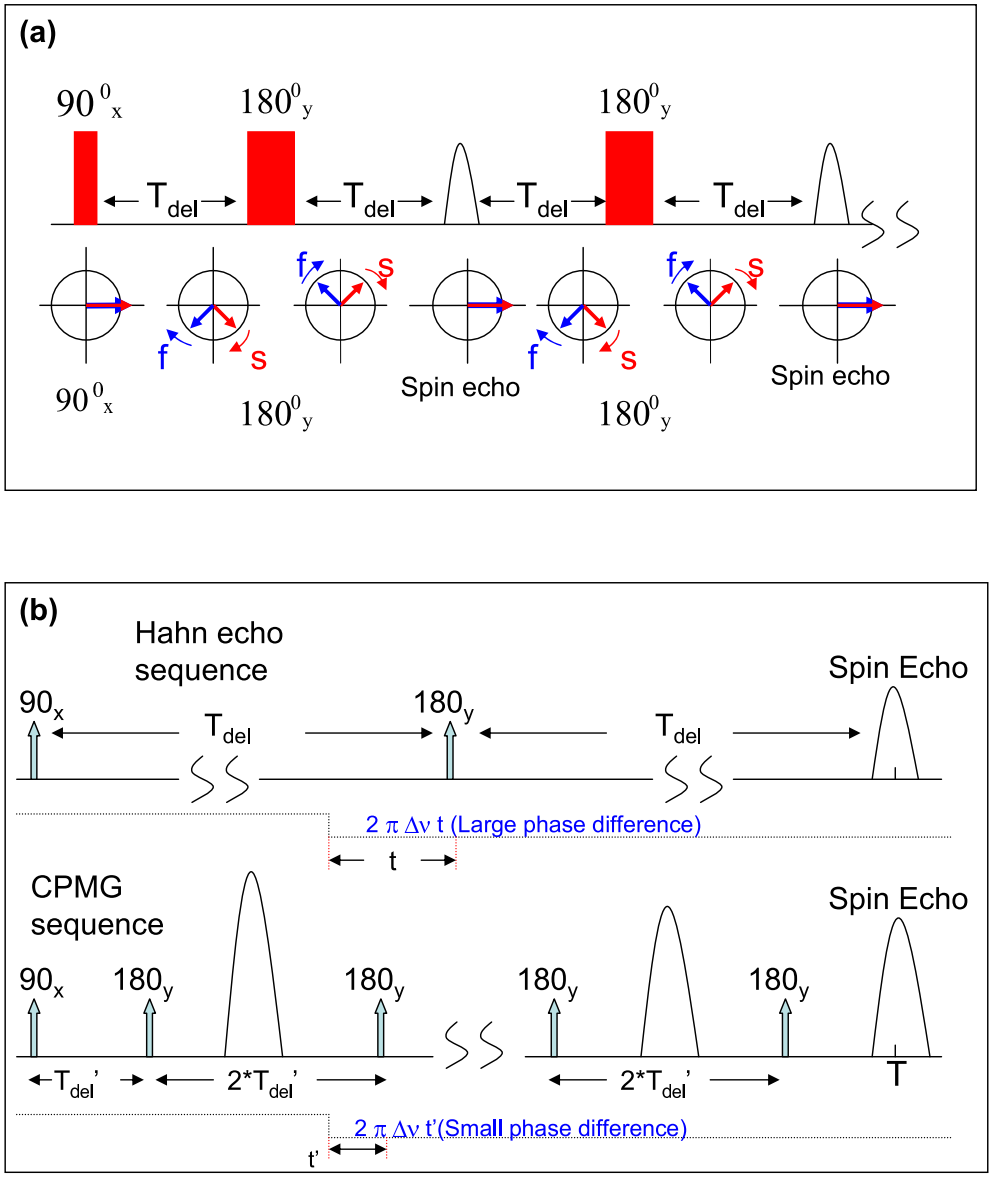

Fig. 10. (a) Carr-Purcell-Meiboom-Gill (CPMG) sequence; (b) Comparison of Hahn-echo sequence with CPMG sequence. Phase loss for spin-echo sequence is larger than phase loss of CPMG sequence. Thus when spin echo is observed at time T for both Hahn echo and CPMG sequences, the amplitude of spin echo seen by CPMG sequence is larger.

CHAPTER IV

EXPERIMENTAL APPARATUS

In this chapter, I will briefly describe the instruments and computing program package we used to perform NMR, resistivity, specific heat measurements and electric field gradient (EFG) calculations for this study.

A. NMR Spectrometer

An NMR spectrometer is the major instrument we used for this study. NMR experiments were performed at a fixed field of 9 T using a homebuilt pulse spectrometer [41], and which could cover a temperature range from 1.9 K to 500 K. Our NMR instrument has several key components: a 9 T superconducting magnet, pulse sequence generator (PSG), the transmitter, the receiver, the probe, and the cryostat system.

The PSG can produce a short duration pulse used to excite the nuclei whose resonance frequency is near the pulse frequency. It is controlled by a computer programmer written in the LabView language. Through executing a certain pulse sequence by the programmer, the PSG is able to generate pulses with lengths as desired, time the pulses, and switch on and off the decoupler.

The transmitter is used to deliver the RF to the sample to perturb the nuclear spin system from its equilibrium state. RF is produced by a commercial frequency synthesizer which can generate a frequency from 0.1 Hz to 160 MHz. The phase of the RF can be adjusted to generate an H_1 field in $+x$, $-x$, $+y$, or $-y$ direction in the rotating frame of reference.

The receiver detects, amplifies, and digitally records the data signal. After being disturbed by RF, the magnetic moment of spin system will relax to its equilibrium state. During that process, it will induce an electric signal in the pick-up coil sur-

rounding the sample. Normally the voltage induced in the pick-up coil is as low as one microvolt, and it has to be amplified before being digitally recorded by the computer.

The probe is used to contain the sample within the magnet and provides the necessary hardware to measure the sample temperature. Also it couples the sample to the transmitter and the receiver in order to permit the excitation and detection of an NMR signal. The circuit of the probe is basically a tunable LC circuit, and the sample coil serves as the inductor of the LC circuit.

A cryostat system is needed to perform low temperature NMR. Liquid Nitrogen (LN_2) and liquid Helium (LHe) are used to perform measurements from 77 K to 300 K, and from 4 K to 77 K respectively. An electrical current provides power to a resistance heater on the probe to achieve the desired temperature. By carefully adjusting the vapor pressure of LHe, we can also perform measurements at temperature as low as 1.9 K.

The NMR field was calibrated using a $Ga(NO_3)_3$ dilute solution as ^{71}Ga zero-shift reference (frequency close to 115 MHz) for Ga NMR, and using a $Al(Cl)_3$ dilute solution as ^{27}Al zero-shift reference (frequency close to 98 MHz) for Al NMR. The samples for NMR measurements were several cubic millimeters, made into powder, and mixed with KBr.

Magic Angle Spinning (MAS) measurements were performed on a Bruker Avance 400 MHz NMR instrument using Al_2O_3 as reference.

B. WIEN2k Calculations and Other Instruments

The Program Package WIEN2k allows us to perform electronic structure calculations of solids using density functional theory (DFT). It is based on the full-potential (linearized) augmented plane-wave ((L)APW) + local orbitals (lo) method, one of

the most accurate schemes for band structure calculations. Ab initio calculation of EFGs was carried out by using the WIEN2k package on PC with 512 Mb RAM.

The Physical Property Measurement System (PPMS) is a variable temperature-field system, designed to perform a variety of automated measurements, including transport, specific heat, etc. In this study, resistivity was measured by a 4 probe method in the temperature range from 2 to 300 K, and the specific heat was measured in the same temperature range, both using a Quantum Design PPMS system.

The research in this dissertation represents a part of a larger group effort. Besides MAS measurements, I did all other NMR measurements myself. I also carried out EFG calculations using the WIEN2k Package. Transport and specific heat measurements were performed by Dr. Rathnayaka from Dr. Naugle's group, using the PPMM system, and MAS measurements were performed at the NMR Facility in the Chemistry Department, while I analyzed the resulting data. I also synthesized many of samples used, as described in the next chapter, performing in addition X-ray and WDS measurements to analyze these samples.

CHAPTER V

EXPERIMENTAL RESULTS AND DISCUSSIONS

Samples for this study are from different sources. $Sr_8Ga_{16}Ge_{30}$ and the low carrier density $Ba_8Ga_{16}Ge_{30}$ sample were prepared in the Nolas group at the University of South Florida. One $Ba_8Ga_{16}Ge_{30}$ sample was prepared by Yang Li from our group. I prepared the rest of samples, including $Ba_8Ga_{16}Ge_{30}$ made by Ga flux method, $Ba_8Ga_{16}Sn_{30}$, and $Ba_8Al_xGe_{40-x}$ with a series of compositions.

A. $Ba_8Ga_{16}Sn_{30}$

1. Sample Preparation

A $Ba_8Ga_{16}Sn_{30}$ sample was prepared by arc-melting technique in an argon environment, following by annealing at 375 °C for four days. X-ray diffraction measurements verified this sample to be pure Type-VIII clathrate with no additional phases. WDS measurement confirmed that the main phase is type-VIII clathrate with a small amount of pure Sn.

2. Measurements and Discussion

The temperature dependence of the electrical resistivity is shown in Fig. 11, which shows semiconducting behavior. The small downturn for the resistivity at zero field is due the small amount of Sn in the sample.

The specific heat was measured for $Ba_8Ga_{16}Sn_{30}$ from 2 to 300 K. The data are shown in Fig. 12 as a plot of C/T^3 vs T. It can be seen clearly that a broad peak centered at 10 K exists. There are three contributions to specific heat, an electronic contribution C_{el}, a phonon contribution which can be modeled at low temperature as

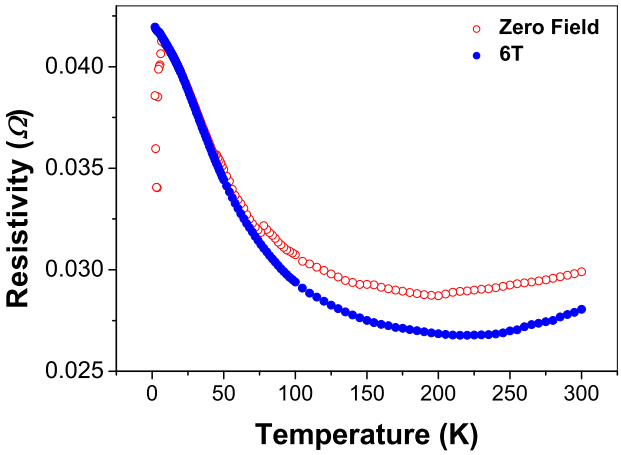

Fig. 11. Temperature dependence of resistivity measured in $Ba_8Ga_{16}Sn_{30}$

a Debye contribution C_D, and an Einstein contribution C_E. The Debye contribution is constant at low temperatures in C/T^3 vs T, however the general T-dependent form for C_D was used in the fit. The electronic contribution to the specific heat is a small portion of the total specific heat at low temperatures. Therefore the peak is mainly from the Einstein oscillation modes. We fit the data to an expression for the specific heat $C/T^3 = \gamma/T^2 + N_E C_E/T^3 + N_D C_D/T^3$ in the temperature range from 2 to 20 K where C_E and C_D are the standard functions [42]. In the fitting, we fixed the numbers of Einstein and Debye oscillators to $N_E = 8$ and $N_D = 46$, respectively, which are the numbers of guest Ba atoms and framework atoms per unit cell respectively. We found $\gamma = 9$ mJ/(mol·K^2), a Debye temperature $\Theta_D = 187$ K, and an Einstein temperature $\Theta_E = 51$ K. These values are similar to a previous report [43]. However, in that paper, a metallic resistivity behavior was seen, whereas our sample shows ordinary semiconductor behavior. Taking these low temperature fitting parameters, we produced curves for the electronic contribution, Debye contribution, and Einstein

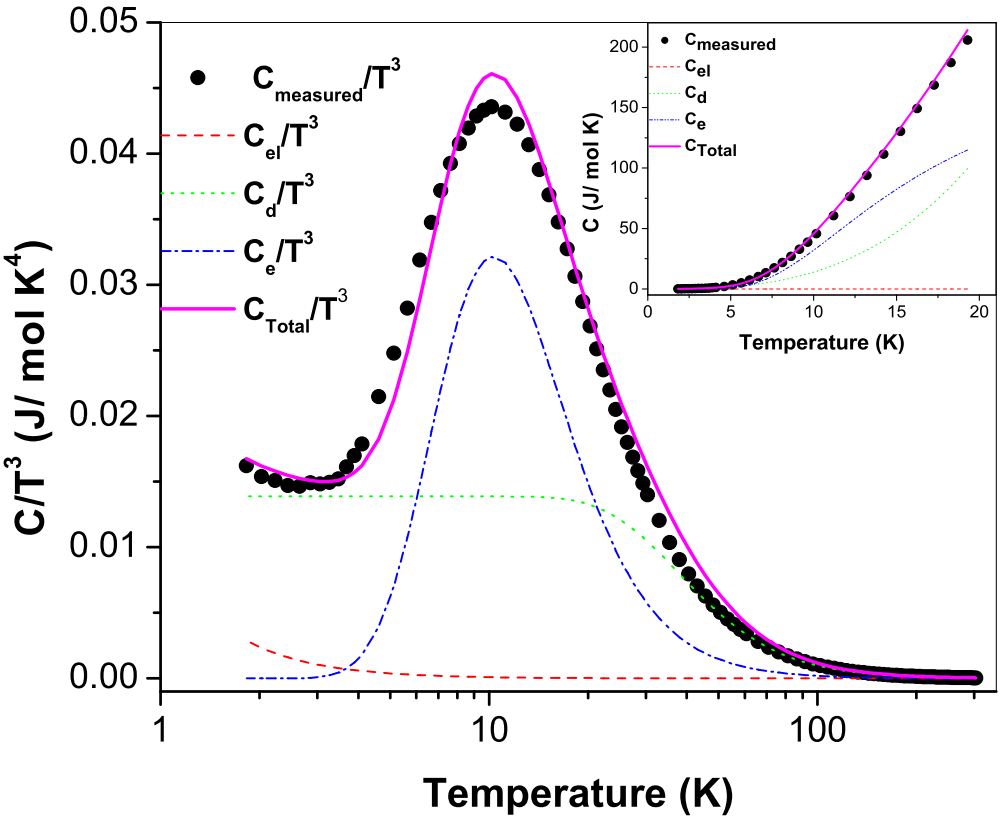

Fig. 12. Temperature dependence of specific heat C of $Ba_8Ga_{16}Sn_{30}$, where $C_{total} = C_d + C_e + C_{el}$ (See text for details)

contribution for the whole temperature range. The results are shown in Fig. 12. We can see there is a good agreement between experimental and calculated results. As I have described in the introduction, the "rattler" is a feature of $Ba_8Ga_{16}Sn_{30}$ clathrate, which is verified by the specific heat study.

B. $Sr_8Ga_{16}Ge_{30}$

1. Sample Preparation

The $Sr_8Ga_{16}Ge_{30}$ sample was prepared by the Nolas group as follows [6]: stoichiometric quantities of the high purity constituent elements were mixed and reacted in pyrolitic boron nitride (BN) crucibles for twenty-four hours at 950 °C then annealed at 700 °C for twenty-four hours. The BN crucibles were themselves sealed inside a fused quartz ampoule, which was evacuated and backfilled with nitrogen gas to a pressure of two-thirds of an atmosphere. The ingots were composed of crystallites with dimensions of one to three cubic millimeters. The ingots are stable in air and water but were etched with aqua regia for metallographic analysis, which indicated single-phase material. X-ray diffraction measurements were used for further characterization, which verified the crystallinity and phase purity of the specimen.

2. Measurements and Discussion

NMR spectra of $Sr_8Ga_{16}Ge_{30}$ at room temperature and 4.2 K are shown in Fig. 13, measured by echo integration. A room-temperature search over a considerably wider range of shifts verified this broadened line to be the only observable signal. Since it is known [44] that Ga occupies all three crystallographic sites in $Sr_8Ga_{16}Ge_{30}$, the single NMR line observed at both temperatures is presumably due to a superposition of signals from these three sites, with their individual powder patterns.

Measured signals correspond to the central-transition, (-1/2↔1/2), for I=3/2 ^{71}Ga, which was confirmed by comparing the pulse length for the $Ga(NO_3)_3$ solution with those of the $Sr_8Ga_{16}Ge_{30}$ sample [45]. This situation is not uncommon in alloy samples, for which random quadrupole couplings can leave the satellite transitions broadened into a featureless background, with the relatively narrow central transition

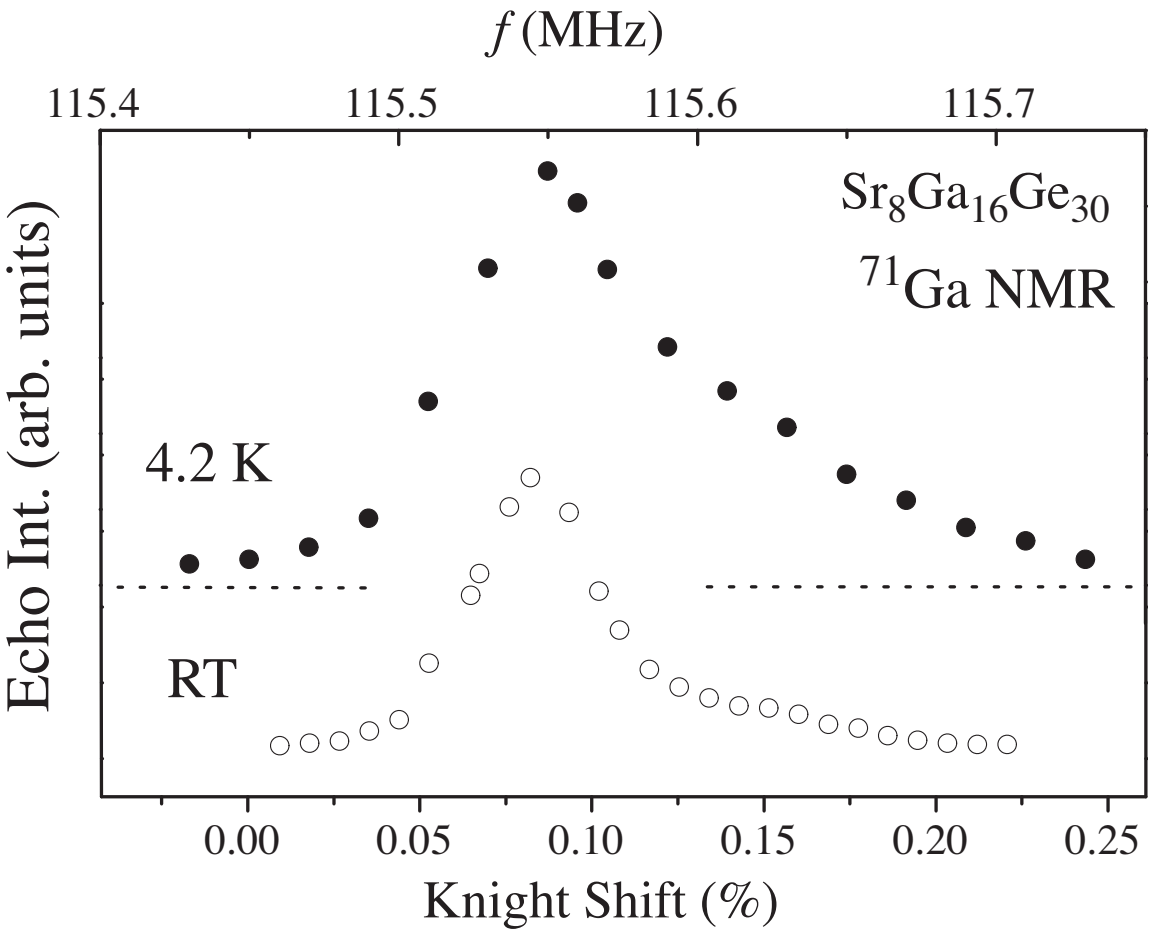

Fig. 13. Lineshapes at room temperature and 4.2 K, offset vertically for clarity

affected only to second order in the quadrupole coupling. T_1 measurements were performed at the center of the lineshape. The data were fitted to a multi-exponential relaxation curve by Eqn. 3.10 assuming magnetic relaxation for the central transition to obtain T_1. The data agreed well with these curves over the whole temperature range. The T_1 results are shown in Fig. 14. These data obey the Korringa relation, a signature of metallic behavior [32], with $T_1 T = 8.5$ sK obtained by least squares fitting. The Knight shift of the center of mass of the lineshape is almost independent of temperature around $K = 0.084\%$ (Fig. 14 inset). These results indicate that T_1 and K are dominated by interactions with conduction electrons, and that $Sr_8Ga_{16}Ge_{30}$ is doped into the metallic regime. This is in agreement with electrical transport for this material [5, 47, 9], which typically indicates n-type behavior, and carrier densities in the range 10^{20} to 10^{21} cm^{-3}, due apparently to intrinsic defects.

Combining the observed T_1 and K to form the Korringa product yields $K^2 T_1 T = 5.9\times10^{-6}$ sK. The free-electron value for ^{71}Ga is 2.73×10^{-6} sK, obtained from Eqn. 2.12. The observed Korringa product is enhanced by a factor of approximately 2.2, which is typical of ordinary metals, and indicative of normal metallic behavior. By contrast the Korringa product in disordered systems containing localized electrons will be strongly enhanced [35, 36], a signature of the effects of the strong correlations [37, 38]. Note that in $Na_xBa_ySi_{46}$ clathrate, a similar modest Korringa enhancement has been observed [46]. However, in that case, K is temperature dependent, indicating possible sharp features in the electronic structure [31], for which there is no evidence in the present case.

For further analysis, we used a parabolic band approximation to estimate K. We assume a spherical Fermi surface, with a conduction band s-orbital fraction equal to 1/4 (corresponding to sp^3 hybridization), $m^* = 3m_e$, and $n = 1.5\times10^{20}$ cm^{-3}, which are typical values for samples of this material [47], and the hyperfine field for Ga,

H_{HF}=620 T [34]. These values yield $K = 0.2\%$, which is slightly larger than observed. Thus, the relatively small K is consistent with the accepted electrical properties of $Sr_8Ga_{16}Ge_{30}$. Note that the quantity which we identify as K is actually an average of individual K values from among the three crystallographically inequivalent framework sites, because of the overlapping of lines. NMR lines for these sites can be seen individually in ^{29}Si NMR [46] or possibly partially separated by magic angle spinning in Ga NMR [48].

The second-order quadrupole coupling can give further line shifts for the central transition, as well as broadening the line. To analyze for this effect, we performed ^{69}Ga NMR measurements at room temperature. We found that the center shift is 0.085% for ^{69}Ga, compared to 0.084% for ^{71}Ga. ^{69}Ga has a quadrupole moment $Q = 0.178\times10^{-28}$ m^2, compared to 0.112×10^{-28} m^2 for ^{71}Ga, and the second order quadrupole shift is proportional to Q^2 [32]. The small observed difference is comparable to the experimental error, and indicates that the second order quadrupole contribution to this shift is very small. This justifies the approximation used above, in which the center shift was interpreted as a Knight shift, of magnetic origin. Furthermore, we found that the linewidth for ^{69}Ga exceeds that of ^{71}Ga, with a ratio of the full-widths at half maximum equal to 2.34, which is slightly smaller than the ratio, $(Q^{(69)}/Q^{(71)})^2 = 2.53$, expected for broadening due entirely to the second order quadrupole coupling. This indicates that the broadening can be attributed mostly to quadrupole coupling, with a small additional anisotropic or inhomogeneous magnetic contribution.

The temperature dependence of the ^{71}Ga linewidth, obtained by calculating the square root of the second moment of the measured line, is shown in Fig. 15. The measured data for this calculation were obtained by Fast Fourier Transform (FFT) of the spin echo, which was obtained using shortened pulses to enhance the observation

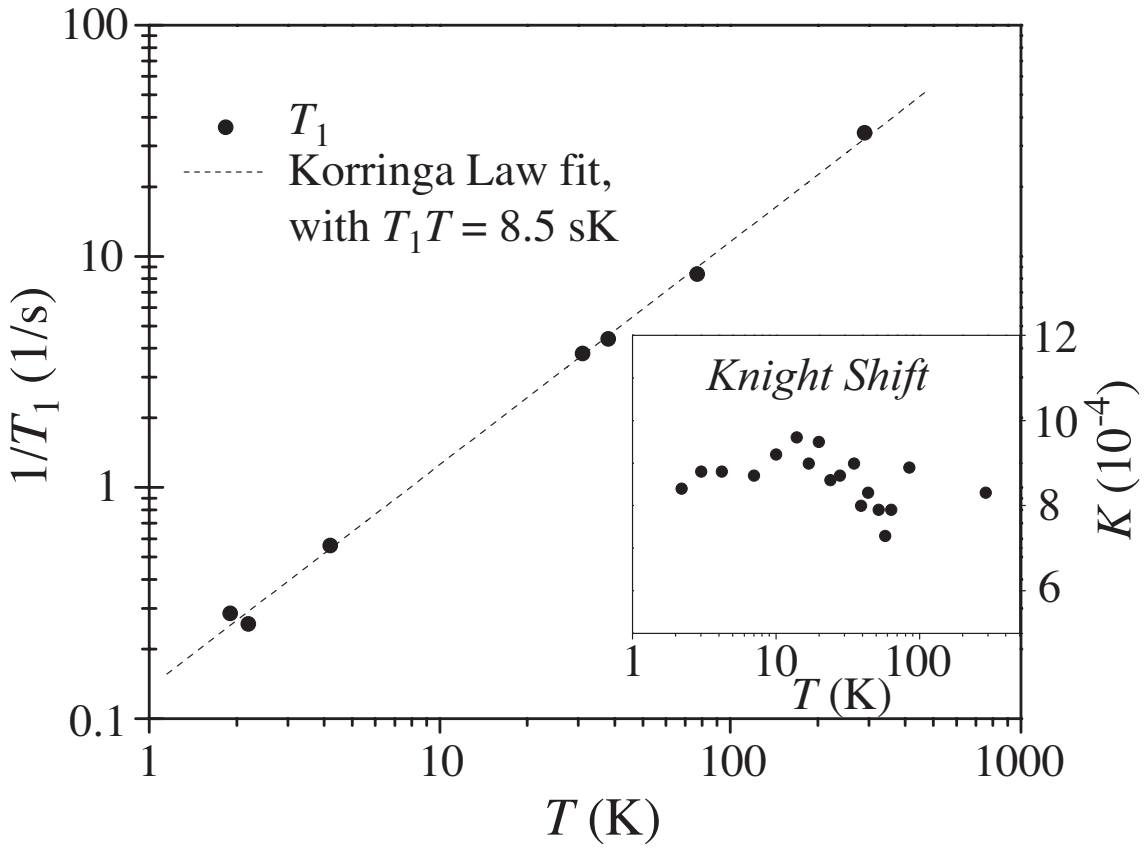

Fig. 14. Temperature dependence of ^{71}Ga T_1; experimental error bars are smaller than the symbol sizes. Dotted curve is a least squares fit to the Korringa Law. Inset: Knight shift of the center of mass, vs. T

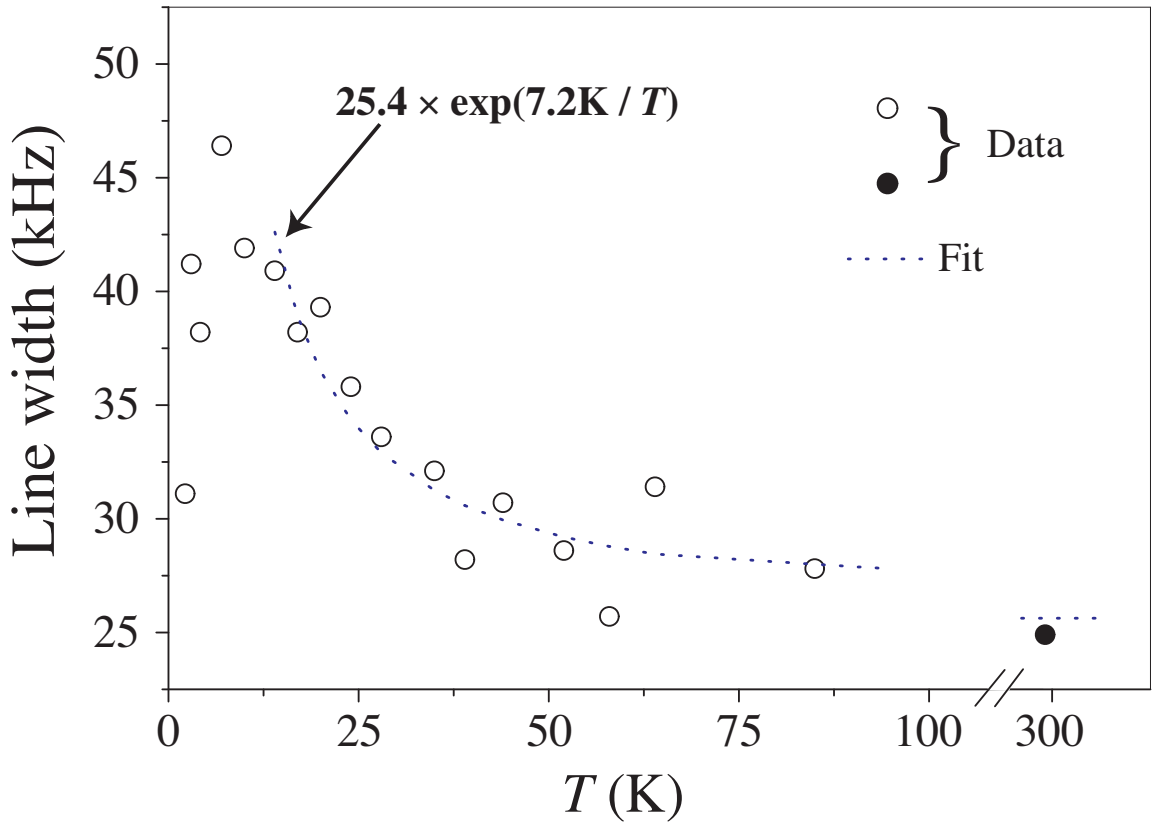

Fig. 15. ^{71}Ga NMR linewidth (square root of second moment) versus temperature, with activated fit described in text

range. There is a significant increase in the linewidth at low temperatures (above 4 K). This change is apparently not due to an electronic structure change since K and $K^2 T_1 T$ do not change. Instead, this change can be attributed to atomic motion. For this mechanism, assuming that the reduced high-temperature width is due to motional narrowing, the relevant timescale can be estimated by 1/linewidth, roughly 10^{-5} s, since this is the timescale for narrowing of an NMR line. This is very slow compared to thermal vibration rates, for example 10^{12} Hz for the Einstein mode of guest atoms in the relatively open type-I clathrate cages [5].

For random hopping, the linewidth can be related to a correlation time, which will follow $\tau_c = \tau_\infty \exp(E_a/kT)$ in the case of an activated process, where E_a is the

activation energy of the system. Motions of atoms in the near vicinity of the Ga nuclei being observed will cause changes in the electric field gradient, and thus shifts in the NMR resonance position, due to the electric quadrupole effect. Because of the superposition of many orientations, we can see only a broadening, rather than a splitting or shift. In the motionally narrowed limit, the excess linewith is proportional to τ_c, so that the linewidth can be fitted to $W_c = W_\infty \exp(E_a/kT)$ to find E_a. Fitting this expression to the high-T tail we find that E_a is 7.2 K. This fitted curve is shown in Fig. 15.

As a further measure of the dynamics, the spin-echo decay was measured by use of the standard Hahn spin echo sequence. The results are shown by Fig. 16. The data were fitted by

$$S = A\{\alpha \exp(-t/T_{2e}) + \exp[-(t/T_{2g})^2]\}. \tag{5.1}$$

Generally, an exponential decay is observed where motion is important, while Gaussian decay is characteristic of the static NMR line, dominated by the nuclear dipole-dipole or pseudo-dipolar couplings [33]. Thus the ratio α is a measure of the relative importance of motion.

The fitting results are shown in Table I. At low T, α is large, and the decay curve is exponential, which indicates that the echo decay is dominated by motion. However at high T, α is small, indicating that the motional contribution is averaged out, leaving a Gaussian decay due to like-spin coupling [33]. At high T, fast motion will cause more of the spin-spin coupling to be like-spin in character, which makes T_{2g} shorter. This is consistent with the observed behavior, and thus the picture established above, whereby the NMR line is subject to progressive motional narrowing as the temperature is raised, which agrees with the spin-echo decay results.

In order to further understand the motion process, we performed CPMG mea-

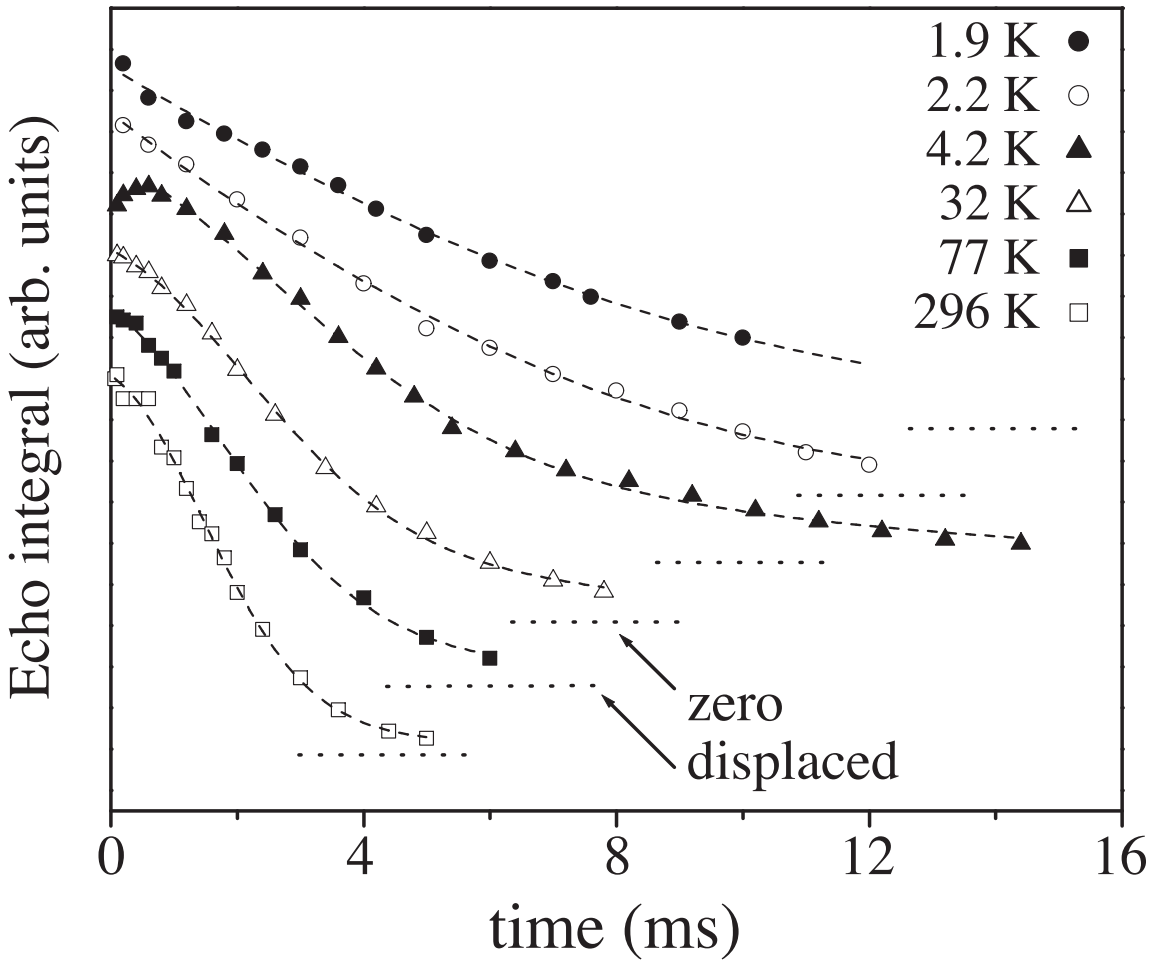

Fig. 16. Spin echo decay rate at different temperatures, with fits described in text

Table I. Fitting result of the spin echo measurements.

Temperature (K)	T_{2e} (ms)	T_{2g} (ms)	α
1.9	8.1±1.5	7.7±3.6	5.0±2.8
2.2	5.6±0.1	7.7±0.1	2.5±0.1
4.2	6.7±0.6	4.6±0.2	1.3±0.4
32	5.2±0.5	3.3±0.1	0.8±0.2
77	3.4±0.4	2.9±0.3	0.8±0.2
296	2.3±0.6	2.2±0.1	0.3±0.1

surements. The results at RT, 77 K, 32 K, and 4.2 K are shown by Fig. 17. We can see that as τ decreases, the echo decay rate becomes smaller, at all temperatures. One common mechanism for this type of decay in a CPMG experiment is diffusion of the atoms under observation. However, since the Ga atoms are bonded to the framework, low-temperature Ga motion seems very unlikely, and indeed we find that the $\exp(-t^3)$ behavior expected in this case [32] does not fit the data very well. Sr-atom motions, however, can slowly modulate the Ga-site quadrupole shifts, providing a decay similar to what we observed. We can not tell solely from these results whether Sr atoms are hopping between cages or between sites within the same cage, however since the energy barrier is evidently quite small, we will assume that these dynamics are associated with the rattling-type motion of Sr within the large cage, as has been discussed previously [5, 6, 9].

To interpret the data, we have invoked a simplified model in which Sr atoms jump randomly between two positions, making nearby Ga nuclei change resonant frequencies by a difference $\Delta\nu$ (See Fig. 18). $\Delta\nu$ will have a range of values according to Ga position and crystal orientation. If we assume the motion is very slow, so that

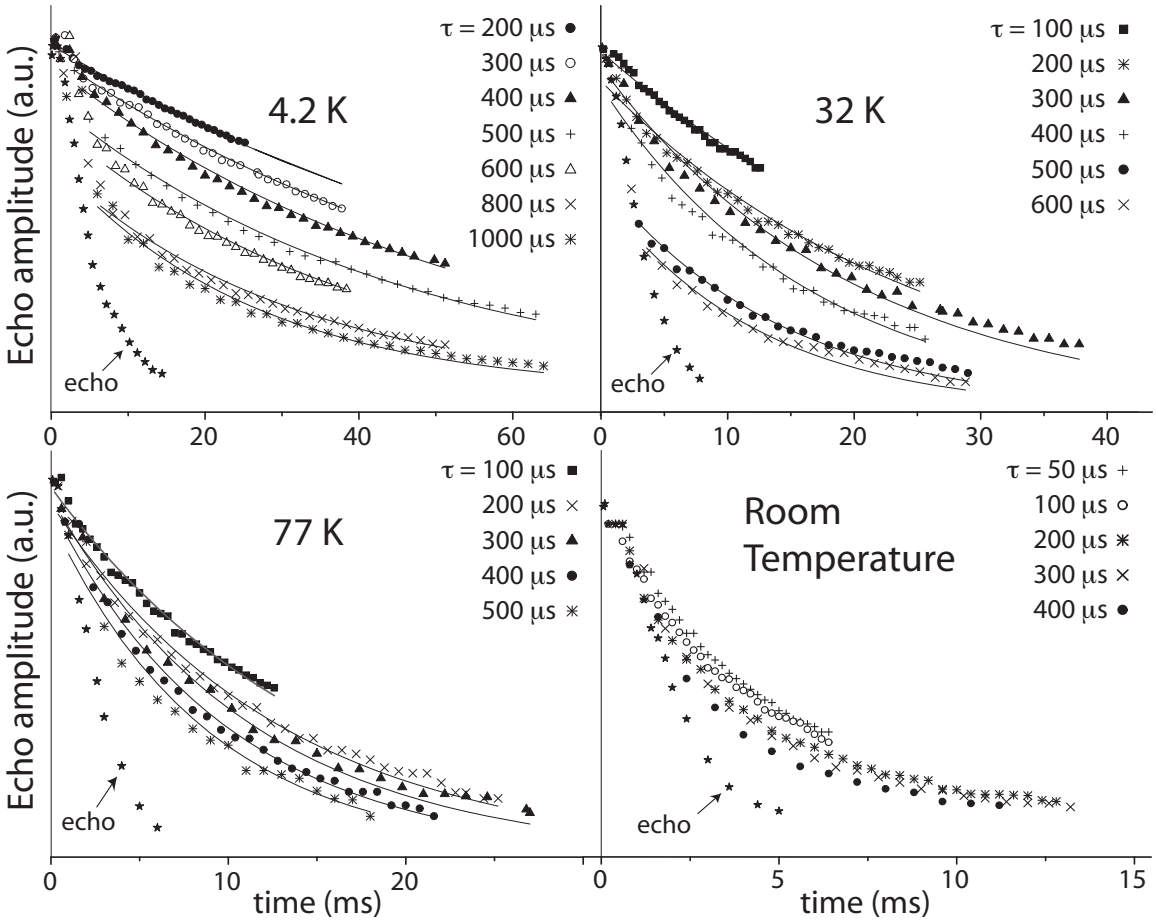

Fig. 17. CPMG measurements at different temperatures. Solid curves for 4.2, 32 and 77 K are fits described in text

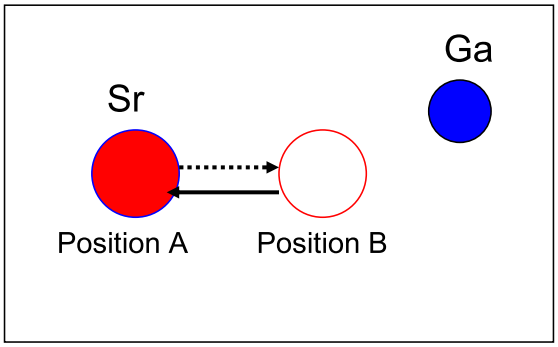

Fig. 18. Illustration of Sr-atom shift, causing a Larmor frequency $\Delta\nu$, for a nearby Ga atom

at most only one jump occurs at time t between 180° pulses, or between 2τ, then the signal at 2τ can be approximately written as

$$S = S_0 e^{-\frac{2\tau}{\tau_c}} + \int_0^{2\tau} dt \frac{S_0}{\tau_c} e^{-\frac{t}{\tau_c}} (e^{-\frac{2\tau - t}{\tau_c}}) cos\psi(t), \tag{5.2}$$

where τ_c is the correlation time, $e^{-\frac{2\tau}{\tau_c}}$ is the probability of no jumping, and $\psi(t)$ $= 4\pi\Delta\nu t$ is the coherence phase loss due to jumping. In this equation, we assume $2\tau \ll \tau_c$, which is reasonable assumption for the present case, because the motion is slow as established. In Eqn. 5.2, the first term is the contribution from nuclei which experience no jump, and the second term is the contribution from nuclei which experiencing one jump. The integration in Eqn. 5.2 can be evaluated. If we further assume $2\pi\tau_c\nu \gg 1$, to the firt order, we will get

$$S \approx S_0 e^{-\frac{2\tau}{\tau_c}} (1 + \frac{2sin(2\pi\Delta\nu\tau)}{\Delta\nu\tau_c}). \tag{5.3}$$

Instead of single echo, we will make N echos as in the CPMG measurements. The signal at time $2\tau N$ will be the power N of the right side of Eqn. 5.3. Now if we assume $\Delta\nu$ has an exponential distribution of the form $P(\Delta\nu)$=exp(-$\Delta\nu/\nu_1$)/ν_1, we find that the spin echo amplitude can be expressed as

$$S = A \exp(\frac{-t}{T_2}) \exp(\frac{-t}{\tau_c}) [1 + \frac{\arctan(2\pi\nu_1\tau)}{\pi\tau_c\nu_1}]^{\frac{t}{2\tau}}, \tag{5.4}$$

where T_2 is the spin-spin relaxation time, and A is constant. In the CPMG experiments, the motion-free decay rate ($1/T_2$ in Eqn. 5.4) in fact differs from the normal spin-spin T_2, since spin locking leads to a lengthened decay time close to T_1 (it is essentially $T_{1\rho}$ [32]). Spin-locking can be eliminated by the use of a phase-alternating pulse sequence (PAPS) [49], however measurements using a PAPS in our case yielded ill-formed echoes, due to the superposition of stimulated echoes [50]. Stimulated echoes can be minimized by perfectly-set 180° pulse, however the large linewith makes this

Table II. Fitting result of CPMG measurements.

Temperature (K)	T_2 (ms)	τ_c (ms)	ν_1 (kHz)
4.2	100	9.2	0.15
32	44	3.6	0.15
77	18	3.2	0.15

difficult in the present case. Therefore, we used the standard CPMG sequence, making the spin-locking T_2 an adjustable variable.

We found that the RT data did not fit Eqn. 5.4 very well, presumably because the high-temperature T_1 is too short to develop complete spin locking. Therefore we fit the data for the other three temperatures to Eqn. 5.4. The fitting results are shown in Table II. The results show that the typical Ga Larmor frequency difference ν_1, which may vary due to the Ga atom's distance from and orientation relative to the moving Sr, is 0.15 kHz. We also fitted the resulting correlation times to the activation energy formula $\tau_c=\tau_\infty \exp(E_a/kT)$. Fig. 19 is the result for this fit, which yields an activation energy E_a=4.6 K. This value is close to the E_a obtained from linewidth measurements.

Zerec et al. [21] have examined a model of azimuthal four-well tunneling for the Eu clathrate, and their experimental resonant ultrasonic data could be fit satisfactorily by considering a four level tunnel system with well-defined barriers that are the same for each cage. However for Sr clathrate, the model did not work well, and the best fit was obtained assuming that the transitions took place between energy levels of the overall harmonic potential well for the Sr atom in its cage. This corresponds to a very large energy difference. In our experiment we find a small energy barrier with value close to 5 K. This is consistent with the thermal conductivity experiments

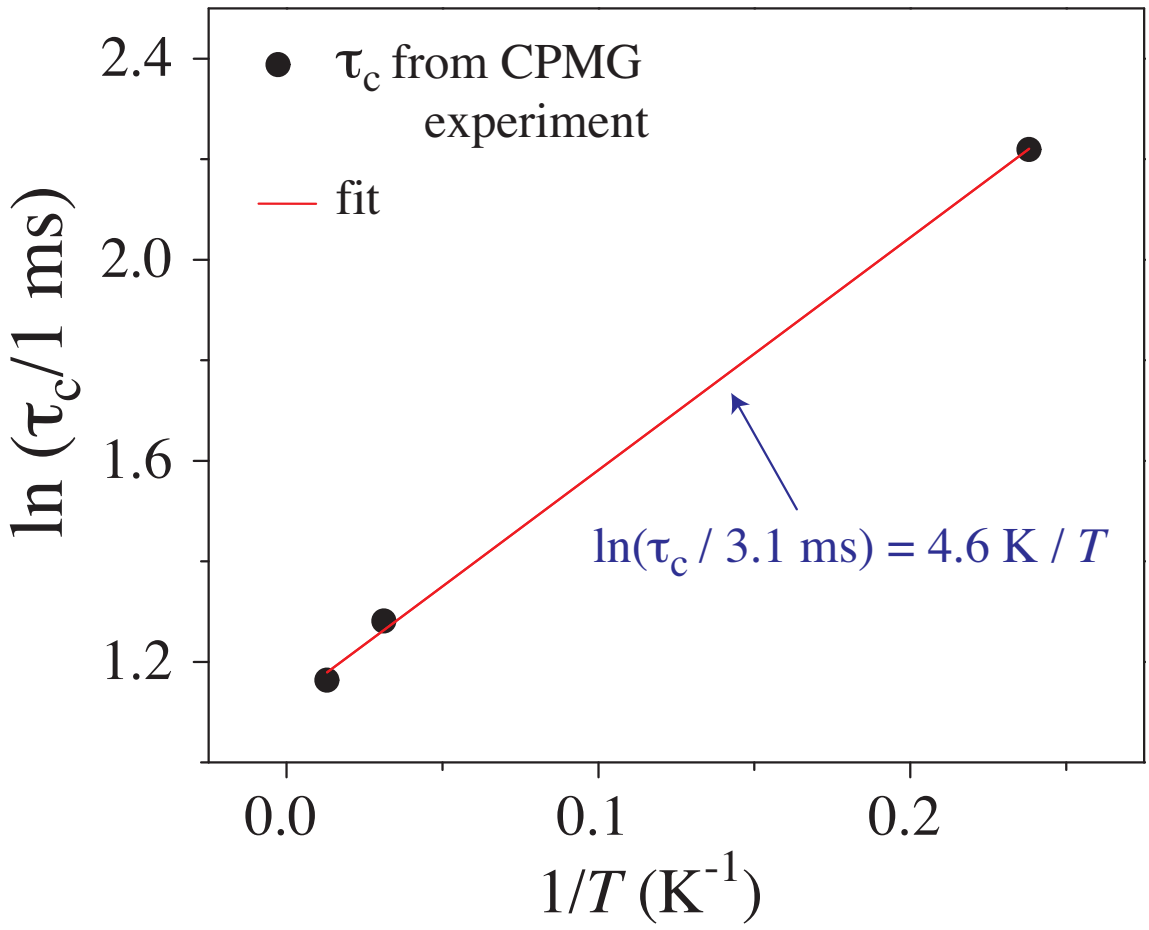

Fig. 19. Correlation time versus temperature (Solid line is the fitting result according to activation energy formula)

[19] observed at temperatures below 1 K, and confirms that transitions between small energy levels play an important role. It is unclear whether this picture also provides a good fit to the resonant ultrasound measurements [21], however clearly there must be higher-energy excitations corresponding to the observed Einstein mode [5, 51, 10], in addition to the lower-frequency fluctuations which have a more prominent effect on the NMR measurements. Thus it seems possible that a model which combines these pictures may be consistent with the resonant ultrasound as well as the NMR results.

A specific heat study has previously been done for $Sr_8Ga_{16}Ge_{30}$ [5]. As in $Ba_8Ga_{16}Sn_{30}$, a "rattler" feature was observed for this Sr clathrate. A Fourier map obtained from neutron diffraction measurements showed that each Sr atom has a displacement roughly 0.3 Å from the center of the cage at low T [20]. In order to approximate the tunneling rates, we first consider a simplified two level system consisting of an infinite square well modified to have a square barrier at its center. For an infinite square well having width 0.6 Å plus a barrier having width 0.2 Å and height 60 K, there are eigenstates with energy 32.2 K and 38.1 K, giving a tunnel splitting of 5.9 K. This is similar to the activation barrier we observed, however the corresponding tunneling frequency is 10^{11} Hz (the splitting expressed in frequency units). This certainly can not correspond to the situation in the Sr clathrate, for which the dynamics include slow motions of the order 10^5 Hz, as evidenced by the NMR. Thus we conclude that the activation energy observed by NMR cannot be a tunnel splitting between symmetric well states.

An asymmetric well can dramatically reduce the tunnel rate [52, 53], and also can explain the linewidth increase with temperature decrease because of different Ga Lamor frequencies for Sr at different sites [32]. Consider a general situation of an asymmetric double well potential with two low-lying states differing by energy Δ, and a potential barrier between them with a tunneling rate $\Delta_0/\hbar$. Fig. 20 is a

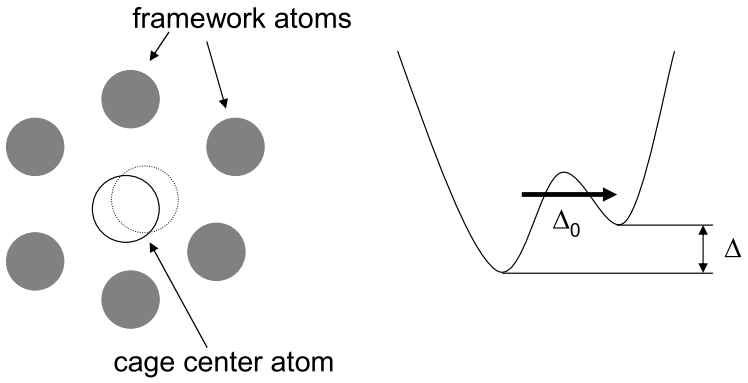

Fig. 20. Right: A two-level system modelled as a double well potential with an energy difference Δ between the two positions, and a tunnelling probability Δ_0 for crossing the barrier between the two metastable states. Left: Physical system corresponding to this potential. Dark solid circles are framework atoms, Ge and Ga. Open circle is cage center atom, Sr.

cartoon of this situation. It can be shown [54] that the energy splitting between the two eigenstates is:

$$\Delta E = \sqrt{\Delta^2 + \Delta_0^2}. \tag{5.5}$$

This is the model often used for Two Level Systems (TLS) in glassy materials. For a symmetric TLS, where Δ=0, the energy splitting of the two states will be the exact tunneling energy. In our systems, we observed a barrier of roughly 5 K, in which case the corresponding tunneling frequency will be 10^{11} Hz. Again this is not what we observed in our experiments. However for an asymmetric TLS, where $\Delta \neq 0$, from the above expression, Δ_0 can be much smaller than ΔE, so the tunneling rate can be dramatically reduced. A broad range of asymmetry parameters is found in many glassy systems, and this is the common way to understand the T^2 behavior of the thermal conductivity.

Thus, we can understand our observations in terms of non-resonant atomic tunneling between asymmetric sites within the cages, in the presence of disorder. There are various possibilities for the source of this disorder. For example, it is known that the Ga atoms are distributed among the different framework sites [44], which will lead to asymmetric on individual cages. Furthermore, Sr vacancies or cage-cage interaction might also contribute. It is true that neutron diffraction measurements show 4 equivalent positions for each Sr atom [20], however this is not inconsistent with an asymmetric well, as long as the asymmetry is randomly distributed, since the scattering experiments do not distinguish static from transient disorder.

One thing that this model can not explain is the linewidth decrease at the lowest temperatures (below 4 K, see Fig. 15). One possible explanation could be that at very low temperatures the displacement of the guest atoms assumes an ordered configuration. A similar result has been found for Si clathrates [55], in which cage-centered sodium atoms are observed to dimerize at low temperatures. A configuration of this type could result in a decreasing linewidth due to decreased strain in the lattice.

3. Summary

Now I would like to briefly summarize the results on $Sr_8Ga_{16}Ge_{30}$. We observed linewidth changes indicating slow atomic motion in the Sr clathrate. CPMG measurements yielded results that are consistent with the linewidth changes. By a simple model, we obtained an activation energy E_a=4.6 K for Sr hopping. This model assumed a wide distribution of hopping rates, and an asymmetric well model worked well to explain the data. The T_1 of $Sr_8Ga_{16}Ge_{30}$ obeys a Korringa relation, implying normal metallic behavior for the Sr clathrate, as expected for a heavily doped n-type semiconductor.

C. $Ba_8Ga_{16}Ge_{30}$

1. Sample Preparation

One of the $Ba_8Ga_{16}Ge_{30}$ samples was prepared by the G. S. Nolas group in the same way as $Sr_8Ga_{16}Ge_{30}$ [6]. Other BaGaGe samples were prepared in our group by arc-melting the elemental constituents, with subsequent solid-state reaction. Structural refinement was carried out using the General Structure Analysis System (GSAS) software package [56, 57]. Powder x-ray diffraction patterns show that samples are single phase plus a small amount of unreacted Ge in some cases [58]. A Ga flux sample was prepared by starting with $Ba_8Ga_{30}Ge_{30}$, following by arc-melting and annealing, after which the sample was put into HCl for 2 days to remove excess Ga. For this sample, powder x-ray diffraction patterns show that the main phase is type-I clathrate with a minority Ga metal phase. A EDS (energy dispersive spectroscopy) measurement on the Ga flux sample is shown in Fig. 21. Analysis of the scans confirmed the clathrate main phase.

2. Measurements and Discussion

All NMR spectra were measured by echo integration. We observed a generally featureless Ga NMR lineshape due to a superposition of signals due to the different Ga sites [44], with their individual powder patterns. Measured signals correspond to the central-transition, (-1/2↔1/2), for I=3/2 ^{71}Ga, which was confirmed by comparing the pulse length for a $Ga(NO_3)_3$ aqueous solution with those of the samples [45]. Thus the spectra are very similar to these observed in $Sr_8Ga_{16}Ge_{30}$. T_1 measurements were done at the center of the lineshape. The data were fitted to a multi-exponential relaxation curve by Eqn. 3.10 assuming magnetic relaxation for the central transition to obtain T_1. The data agreed well with these curves over the whole temperature

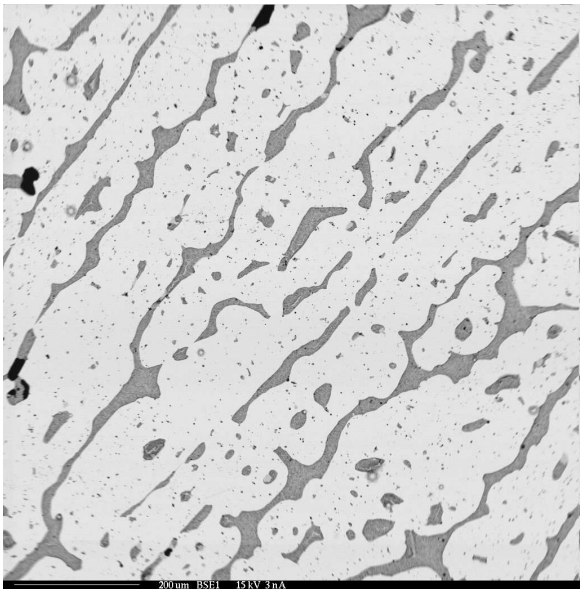

Fig. 21. EDS scan of $Ba_8Ga_{16}Ge_{30}$ made by Ga flux method (Light grey is clathrate phase, dark grey is Ga metal)

range.

$Ba_8Ga_{16}Ge_{30}$ samples prepared with stoichiometric starting materials are always n type [5, 60], while $Ba_8Ga_{16}Ge_{30}$ samples prepared from Ga flux are always p type [8, 29, 24]. We will first discuss NMR results for two n type $Ba_8Ga_{16}Ge_{30}$ samples prepared with stoichiometric starting materials. One sample labelled as sample GN was prepared by the G. S. Nolas group and another labelled as sample YL was prepared by our group. Sample GN has been carefully measured by the Nolas group, and the measurements yield carrier density $n = 8.7\times10^{19}\text{cm}^{-3}$, resistivity $\rho = 41$ mΩ·cm, and Seebeck coefficient S = -141 μV/K. Since the Seebeck coefficient is negative, it confirms that sample GN is n type. Sample YL proved to be too fragile for transport measurement, but to have higher carrier density than sample GN based on the NMR results.

The temperature dependences of the linewidth results are shown in Fig. 22. The linewidth was obtained by measuring the full width half maximum (FWHM) of the spectra. At room temperature, the linewidth of sample GN is 54 KHz, which is narrower than that of sample YL with the value of 67 KHz. In both samples, we observed a linewidth increase with temperature decrease, and at 4.2 K the linewidth of both samples reaches 78 KHz. The temperature dependence of the Knight shift is shown in Fig. 23. The Knight shift was calculated from the peak position of the spectra. We found that the Knight shift change with temperature is very similar to that of the linewidth. The Knight shift of both samples increases with temperature decrease, and reaches the same value at low temperature. Fig. 24 shows the temperature dependence of T_1T. Because the relaxation rate is related to the number of electrons involved in the relaxation process, a higher carrier density results in a faster relaxation process, which corresponds to a shorter T_1. T_1 of sample YL is shorter than that of sample GN, which indicates that the carrier density of YL is higher than that of sample GN. We found that T_1T of both samples is not a constant over the whole temperature range, a deviation from the Korringa relation. However, sample YL has a small deviation, and sample GN has a larger deviation. Fig. 25 shows the temperature dependence of K^2T_1T. K^2T_1T of sample YL is almost constant with a value around 8×10^{-6} sK. Comparing to 5.9×10^{-6} sK for $Sr_8Ga_{16}Ge_{30}$ in the previous section, and 2.73×10^{-6} sK for ^{71}Ga in a free-electron system (from Eqn. 2.13), we see that there is a small enhancement for sample YL. The nearly constant T_1T and small enhancement of K^2T_1T are typical of normal metallic behavior [32]. However for sample GN we found that not only is the K^2T_1T not constant, but it also has very large value, around 40×10^{-6} sK at high temperatures.

Although sample YL deviates from the Korringa relation, it still shows rather typical metal-like properties, such as small enhancement of K^2T_1T by a factor of 2.9.

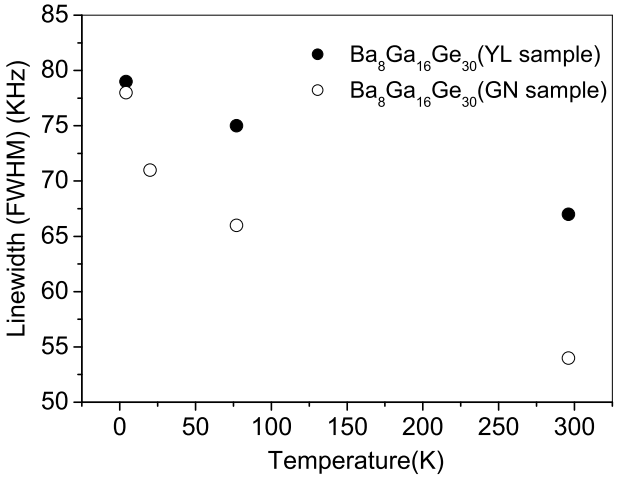

Fig. 22. Temperature dependence of ^{71}Ga linewidth of $Ba_8Ga_{16}Ge_{30}$ samples

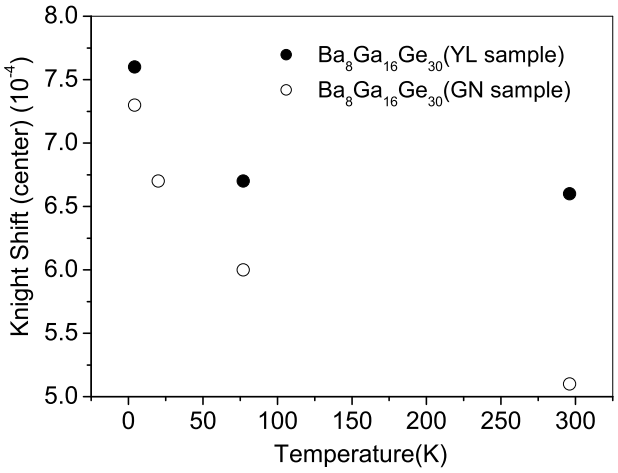

Fig. 23. Temperature dependence of Knight shift of $Ba_8Ga_{16}Ge_{30}$ samples

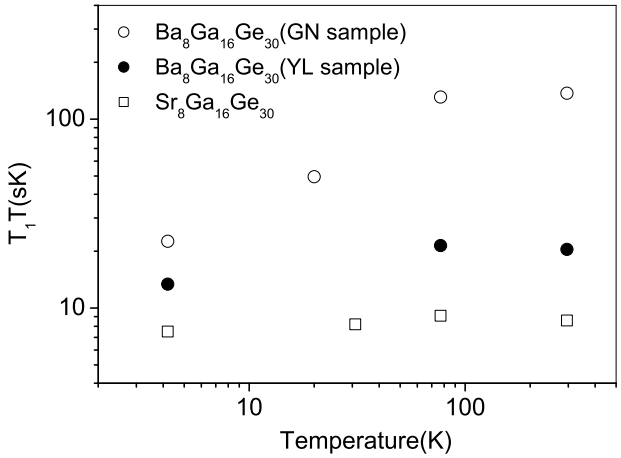

Fig. 24. Temperature dependence of ^{71}Ga T_1T of $Ba_8Ga_{16}Ge_{30}$ samples and $Sr_8Ga_{16}Ge_{30}$ sample

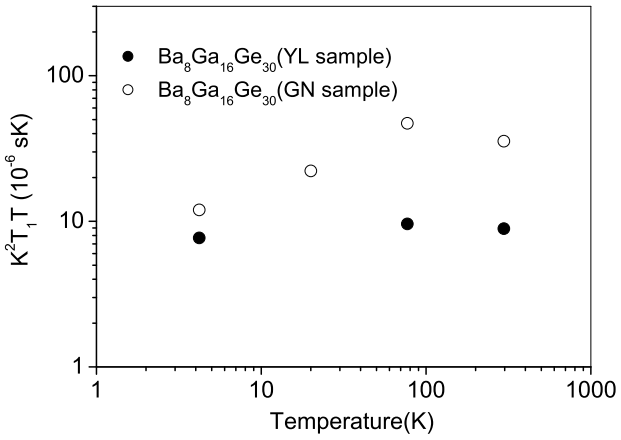

Fig. 25. Temperature dependence of ^{71}Ga K^2T_1T of $Ba_8Ga_{16}Ge_{30}$ samples

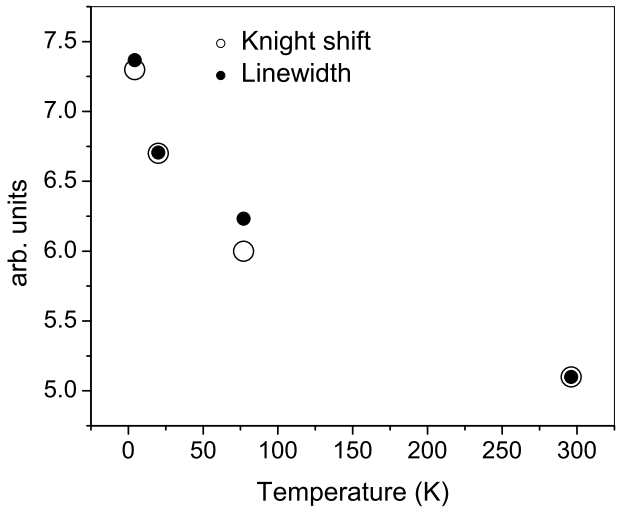

Fig. 26. Temperature dependence of ^{71}Ga Knight shift and linewidth of $Ba_8Ga_{16}Ge_{30}$ sample GN

As to sample GN, the deviation from the Korringa relation is very large, and there is more deviation from metal-like behavior. These NMR results could be explained by carrier freezout in the Ba clathrates with temperature decrease. In the case of carrier freezout, nuclear spins will relax faster due to the interactions localized carriers, which will make T_1 relatively shorter, thus deviating from the Korringa relation.

Considering the standard picture of a disordered band edge in a semiconductor [59], there is a region near the band called the mobility edge, which is the dividing line between localized and extended states. As the number of carriers is reduced, ϵ_f can be lowered into this region. $Ba_8Ga_{16}Ge_{30}$ typically has native donors (presumably due to stoichiometry) [5, 60], which dope the material into the metallic region. However, we see that a relatively high-quality sample such as sample GN is rather close to the localization limit, and this indicates the relative importance of disorder in this material. Sample YL is doped higher into the band due to a larger number of native

defects, which gives behavior much closer to that of a simple metal as seen by NMR.

For sample GN, to examine the correlation of the temperature dependence of the Knight-Shift and linewidth, we set room temperature value of linewidth equal to the room temperature value of Knight-Shift, and then scaled the linewidth values accordingly, and plotted them together, as shown in Fig. 26. The figure shows that the temperature dependence of the Knight-Shift and linewidth are closely related, which indicates an inhomogeneous spin susceptibility. With a tendency toward carrier freezout in the Ba clathrate, and the development of a dilute set of magnetic moments due to these localized carriers, we could explain the linewidth and Knight Shift behavior of both YL and GN samples.

For sample GN, we know the carrier density is $n = 8.7\times10^{19}\text{cm}^{-3}$, the Seebeck coefficient S = -141 μV/K, and the resistivity ρ = 41 mΩ·cm. For metals, the Seebeck coefficient can be expressed approximately as [61]

$$S = N\frac{\pi^2 k^2 T}{3eE_f}, \tag{5.6}$$

where N is the number of minima at the band edge (e.g. $N = 6$ for silicon), e is the charge of an electron, and E_f is the Fermi energy. Given the parabolic band approximation, the Fermi energy can be written as

$$E_f = \frac{1}{2m^*}\frac{\hbar^2(3\pi^2 n)^{\frac{2}{3}}}{N^{\frac{2}{3}}}, \tag{5.7}$$

where m^* is effective mass. From this we get

$$(\frac{m^*}{m_e})N^{\frac{5}{3}} = (4.985\times10^{-14}Km^2/V)n^{\frac{2}{3}}S. \tag{5.8}$$

Band calculations show that the conduction band minimum is in the 110 direction for $Ba_8Ga_{16}Ge_{30}$ [62], corresponding to N =6, so we use this value.

Given the measured values, and assuming $N = 6$, we obtain $m^*/m_e = 0.07$, and

thereby the evaluation of E_f gives $T_f = 3560$ K. Thus it indeed appears that this material is doped into the metallic regime, since $T < T_f$ for our measurements. Also this justifies using the metallic form of S quoted above (the semiconductor T-dependence is different than the metallic). The values of m^*/m_e found here, and also the native doping levels for samples prepared from stoichiometric starting compositions are in rough agreement with what has been found elsewhere [4, 5].

Using these values, a simple Drude model [42] for resistivity gives a scattering time of $\tau = 7{\times}10^{-17}$ s at room temperature, given 41 mΩ·cm for resistivity. Also we can derive $v_f = 1.3{\times}10^6$ m/s, and thus the scattering length $l = v_f\tau{=}8.6{\times}10^{-11}$ m. Using this value, we can define a dimensionless quantity $k_f l = 0.065$. Shastry and Abrahams considered that $k_f l < 1$ corresponds to the diffusive regime for a Fermi liquid in the presence of disorder [36]; in this regime disorder dominates. Note that the Ioffe-Regel criterion is $k_f l = 1/(2\pi)$, according to which the GN sample would also be in the localized regime as defined by Mott [64]. However disorder typically lowers the conductivity at the metal-insulator transition below what is expected from the Ioffe-Regel criterion; for example in Si:P the threshold value is lowered by a factor of 6 [64]. Thus most likely from the transport values we expect that this sample is just on the metallic side, rather than being an insulator.

The above analysis shows that the established theory for metallic electrons, including the effect of electron-electron interactions, can be applied to the observed room-temperature shifts and relaxation times. The temperature-dependence also is characteristic of a disordered metal, rather than that of a semiconductor going through a metal-insulator transition. The latter behavior is exemplified by the behavior of P-doped Si, where generally K^2T_1T will increase as localization takes hold [65, 66]. There is clearly some degree of carrier freezeout in BaGaGe, as can be seen from the Curie-like behavior seen in Fig. 24. However, the strong decrease in K^2T_1T

for the GN sample as T is lowered implies that most electrons remain metallic, and the behavior corresponds to what is expected for metals in the presence of strong disorder [36, 63]. Indeed, as identified above, transport properties indicate the GN $Ba_8Ga_{16}Ge_{30}$ sample to be in the diffusive metallic regime, consistent with the NMR results. Thus it appears that the native defects in n-type $Ba_8Ga_{16}Ge_{30}$ play a very significant role in the transport behavior, which must be considered if these materials are to be used in applications.

$Ba_8Ga_{16}Ge_{30}$ is electrically very similar to $Sr_8Ga_{16}Ge_{30}$, but diffraction measurements indicate that the Ba atoms remain at the cage centers, in contrast to the Sr behavior. From NMR measurement, we observed different behavior between $Ba_8Ga_{16}Ge_{30}$ and $Sr_8Ga_{16}Ge_{30}$. In Sr clathrate, we observed slow atomic motion [67], and no sign of carrier freezout. For the different samples we have studied, Ga NMR in all $Ba_8Ga_{16}Ge_{30}$ cases exhibits a larger linewidth than in $Sr_8Ga_{16}Ge_{30}$, and the T_1 deviates from a Korringa relation at low temperatures, in contrast to the simple-metallic behavior seen in $Sr_8Ga_{16}Ge_{30}$. There is also a temperature-dependence to the center shift of the Ba-clathrate resonance, not seen in the Sr clathrate. These results are consistent with a tendency toward carrier freezout in the Ba clathrate, and the development of a dilute set of magnetic moments due to these localized carriers, or possibly the presence of narrow features in the electronic density of states, such as exhibited in $Na_xBa_ySi_{46}$ clathrate [31]. This behavior unfortunately has precluded the comparison of Sr motion to the corresponding behavior in the Ba clathrate.

$Ba_8Ga_{16}Ge_{30}$ samples made from Ga flux are alway p type clathrates [8, 29, 24]. NMR measurements of the p type sample show different behavior from the n type samples. Fig. 27 shows that the relaxation rates of both p type and n type $Ba_8Ga_{16}Ge_{30}$ samples deviate from the Korringa relation. $1/T_1$ for the n type sample has a negative curvature, while $1/T_1$ for the p type sample has positive curvature.

Fig. 28 shows that the linewidths for both p type and n type samples increase with decrease temperature, but with different values. Fig. 29 shows that the Knight Shift of the p type sample decreases with decreasing temperature, while the Knight Shift of the n type sample increases with decreasing temperature.

As described in the introduction, we know that Knight shift is mainly due to the interaction of s electrons with the nucleus. In the p type $Ba_8Ga_{16}Ge_{30}$, the main carriers are holes, and most of these holes could be in a p orbital state, like in GaAs, where the valance band-edge states have p symmetry [68]. The contact interaction of p states with the nucleus is zero. Thus it is reasonable to have a smaller Knight shift in p type than in the n type material where the main carriers are electrons. Indeed that is exactly what we observed, and results are shown in Fig. 29. In Fig. 27, we can see that at low temperature, the T_1 of n type deviates from the Korringa law, and T_1 of p type roughly follows the Korringa relation in contrast to the n type case. The difference is due the fact that at low temperature carriers freeze out for n type $Ba_8Ga_{16}Ge_{30}$ as we have discussed early, and for p type sample, since the Fermi energy stays inside of the valence band, carriers do not freeze out in this situation.

3. Summary

Now I would like to briefly summarize the results on $Ba_8Ga_{16}Ge_{30}$. We observed that the relaxation behavior (T_1) deviates from the Korringa relation, and the Knight shift and linewidth change with temperature. These results could be explained by carrier freezout in the Ba clathrate, and the development of a dilute set of magnetic moments due to these localized carriers. NMR studies on $Ba_8Ga_{16}Ge_{30}$ made from Ga flux show different behavior from samples made with a stoichiometric ratio, which is due to the different carrier type among these samples. The sample made from Ga flux is p type, while samples made with stoichiometric ratio are n type. Contact

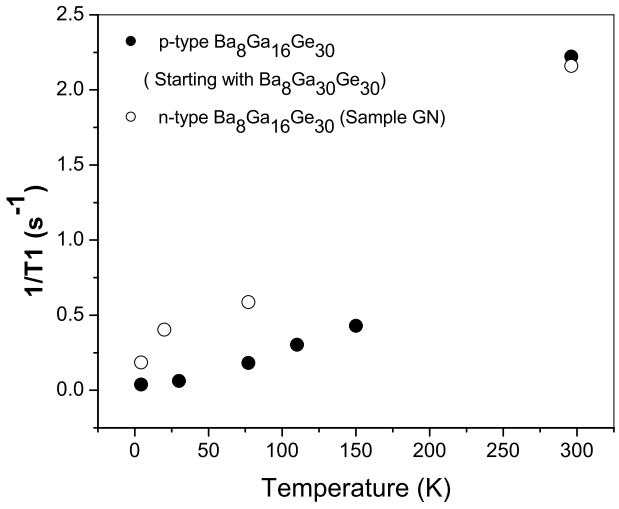

Fig. 27. Temperature dependence of ^{71}Ga $1/T_1$ of p type and n type $Ba_8Ga_{16}Ge_{30}$ samples

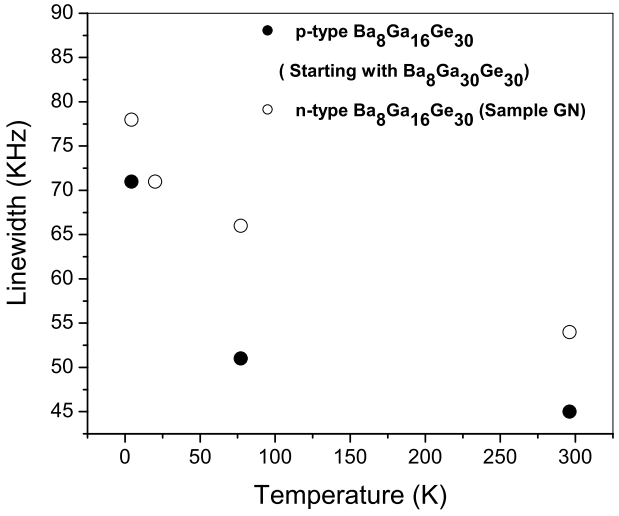

Fig. 28. Temperature dependence of ^{71}Ga Linewidth of p type and n type $Ba_8Ga_{16}Ge_{30}$ samples

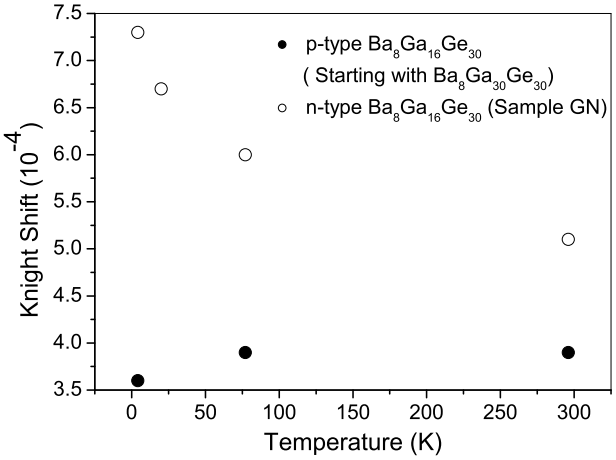

Fig. 29. Temperature dependence of ^{71}Ga Knight Shift of p type and n type $Ba_8Ga_{16}Ge_{30}$ samples

interaction in the n type is apparently stronger, and there is carrier freezout in the n type, but not in the p type clathrates.

D. $Ba_8Al_xGe_{46-x}$

1. Sample Preparation

All Al samples were prepared by the arc-melting technique in an argon environment, following by annealing at 500 °C for two days. X-ray diffraction measurements verified the Al_{13} and Al_{16} samples to be pure Type-I clathrate with no additional phases, and for Al_{12}, the majority phase is Type-I clathrate with very small amount of Ge phase.

2. Measurements and Discussion

WDS (wavelength dispersion spectroscopy) was performed on $Ba_8Al_{10}Ge_{36}$. The results showed that the actual composition is $Ba_8Al_{9.2}Ge_{33.6}[]_{3.2}$, where [] denotes a vacancy. There are roughly 3 vacancies per unit cell, similar to the number of vacancies in Ba_8Ge_{46}. Studies show that Ba_8Ge_{43} is characterized as a defect clathrate of type-I structure with three missing Ge atoms in the covalent Ge framework, where the vacancies of $Ba_8Ge_{43}[]_3$ (space group $Im\bar{3}d$) show a full ordering [69, 70, 71]. Our WDS measurements show that Al-deficient samples retain a similar number of vacancies as in Ba_8Ge_{46}. We do not know whether these vacancies are in an ordered structure. The number of vacancies in Al_{10} sample should be approximately 1.5 as required by the Zintl concept, so it appears that this result does not follow the Zintl concept. $Ba_8Ge_{43}[]_3$ does not follow the Zintl concept either, as there are 4 vacancies instead of 3 required by Zintl concept. However. the latter may be explained as due to reduced charge transfer from Ba to the framework. whereas in $Ba_8Al_xGe_{46-x}$ it is not clear why the vacancy number is unchanged relative to Ba_8Ge_{43}.

^{27}Al NMR spectra of $Ba_8Al_xGe_{40-x}$ with x = 12, 13, and 16 at room temperature are shown in Fig. 30, measured by spin echo integration. A room temperature search over a considerably wider frequency range verified the broadened lines to be the only

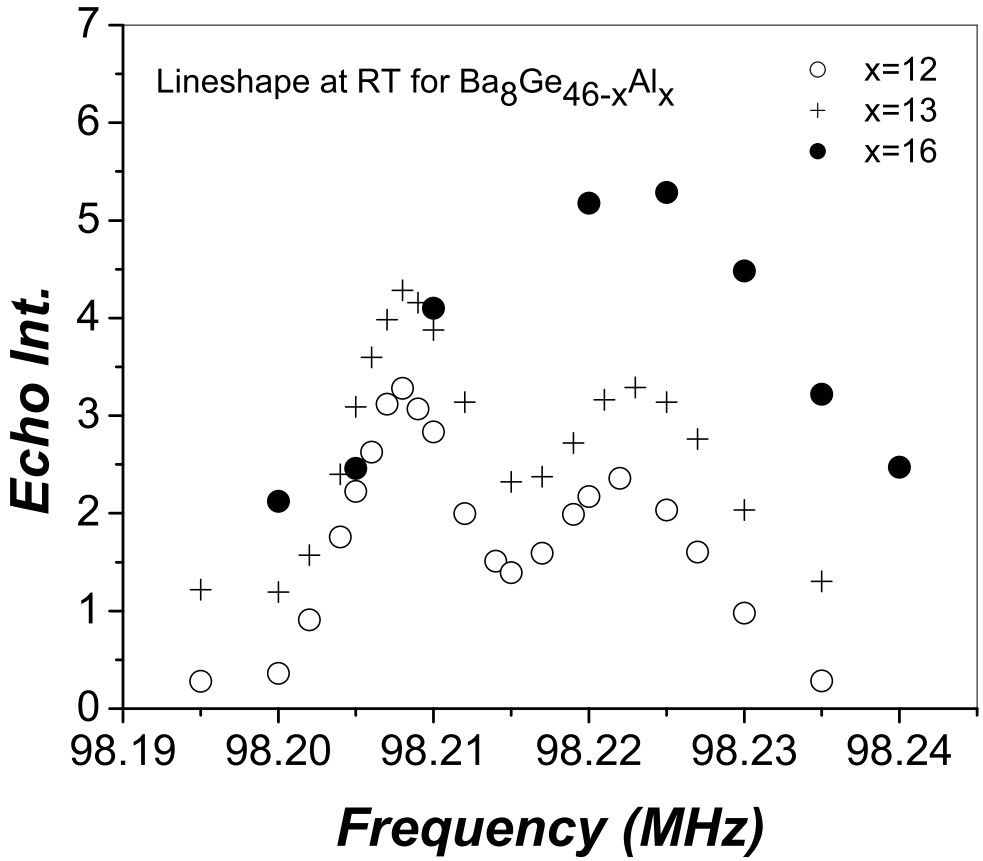

Fig. 30. Lineshapes of $Ba_8Al_xGe_{46-x}$ with x = 12, 13, and 16 at room temperature

observable signal. For type-I clathrates, there are three framework sites with different symmetry and different local environment, and microstructure studies of $Ba_8Al_{14}Si_{31}$ show that Al can occupy any of these three framework sites [73], thus the observed NMR line of Al-Ge systems is presumably due to a superposition of signals from these three sites, with their individual powder patterns. For x = 12 and 13 we observe two obvious peaks, while for x = 16 a single, broader line is seen.

To further understand the origin of these peaks, we measured the frequency dependence of T_1 at room temperature, and the results are shown in Fig. 31 and

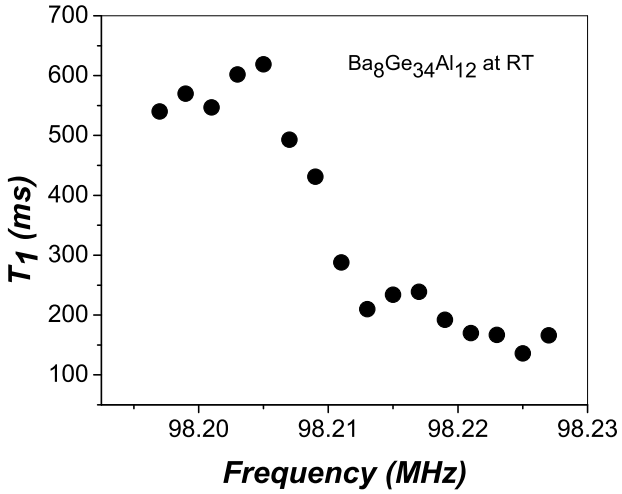

Fig. 31. Frequency dependence of T_1 measurements of $Ba_8Al_{12}Ge_{34}$ sample

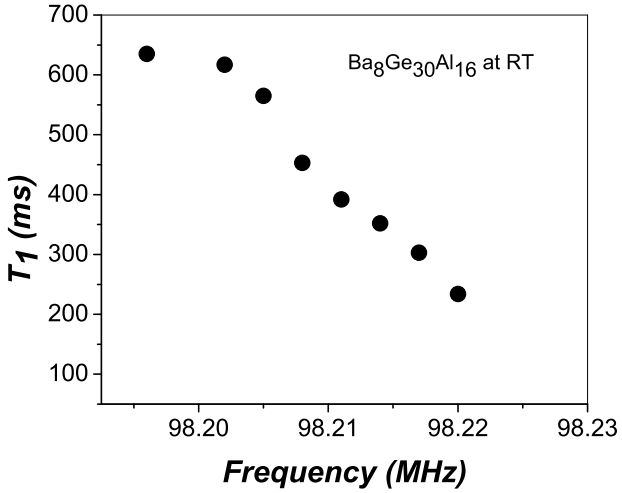

Fig. 32. Frequency dependence of T_1 measurements of $Ba_8Al_{16}Ge_{30}$ sample

Fig. 32. For the Al_{16} sample, T_1 gradually changes with frequency, having a roughly linear relation. The decrease in T_1 with increasing shifts is in line with the Korringa law, and indicates that a distribution of metallic shifts is largely responsible for the broadening. A similar result was observed for ^{71}Ga NMR in $Sr_8Ga_{16}Ge_{30}$. For the Al_{12} sample, T_1 is relatively flat under each of the two peaks, and changes gradually between the two peaks. Thus for this material the two peaks correspond to two distinct sites with different T_1, with little distribution of metallic shift within each peak. Measurements on Al_{13} yielded similar results to those of Al_{12}. With 3 vacancies per formula cell, and each site having 4 neighbors, 12 framework sites will be adjacent to vacancies. With random occupation, 3 out of 9 Al atoms will be located on these sites. Given the valence, it seems reasonable that Al would prefer these sites. Thus we assign the lower NMR peak, which appears in Al_{12} and Al_{13}, to Al next to vacancies, and we find that roughly 1/2 the Al are located on these sites.

We measured the temperature dependence of T_1 and the Knight shift at the peak positions of each lineshape, and the results are shown in Fig. 33, and Fig. 34. T_1 nearly follows the Korringa relation for all Al samples, which indicate that the samples are metallic. The Knight shift of the Al_{16} sample decreases with decreasing temperature, similar to the behavior of p type Ba clathrate which we have discussed earlier. Former group member Yang Li and colleagues in Beijing did band structure calculations for BaAlGe clathrates, and the results show that E_f of $Ba_8Al_{16}Ge_{30}$ is at the edge the valence band, while E_f of Al_{10} is at the edge of the conduction band [72]. The calculation is consistent with the temperature dependence of the Knight shift for a p type sample, such as the p type Ba clathrate. Knight shifts of the low frequency peak of Al_{12} sample increase with decreasing temperature, but the change is much smaller than in Al_{16}. Since the high frequency peak for Al_{12} at low temperature is suppressed, and becomes a shoulder, it is difficult to follow the Knight

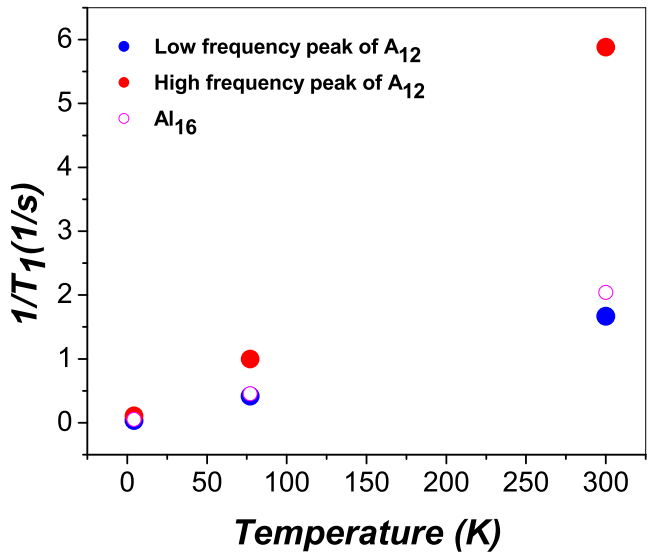

Fig. 33. Temperature dependence of T_1 for the single peak of $Ba_8Al_{16}Ge_{30}$ and two peaks of $Ba_8Al_{12}Ge_{34}$

shift change with temperature for this peak. The Korringa product of the free-electron value for ^{27}Al is 2.33×10^{-6} sK obtained from Eqn. 2.13. At room temperature, the enhancement of the Korringa product for Al_{16} sample is almost 11, and 5 for the Al_{12} sample.

The temperature dependence of the electrical resistivity of the Al_{12} sample is shown in Fig. 35 in the temperature range 2 K to 300K. The resistivity of $Ba_8Al_{12}Ge_{34}$ is roughly half of value of $Ba_8Al_{14}Ge_{31}$ [73], and shows a metallic temperature dependence, which is consistent with NMR measurements.

An NMR lineshape measurement for $Ba_8Al_{12}Ge_{34}$ at 4.2 K is shown in Fig. 36. Compared with the lineshape at room temperature, the high frequency peak at 4.2 K is suppressed, and becomes a shoulder. Furthermore, we could distinguish the quadrupole satellite lines which were not observed at room temperature, due to the

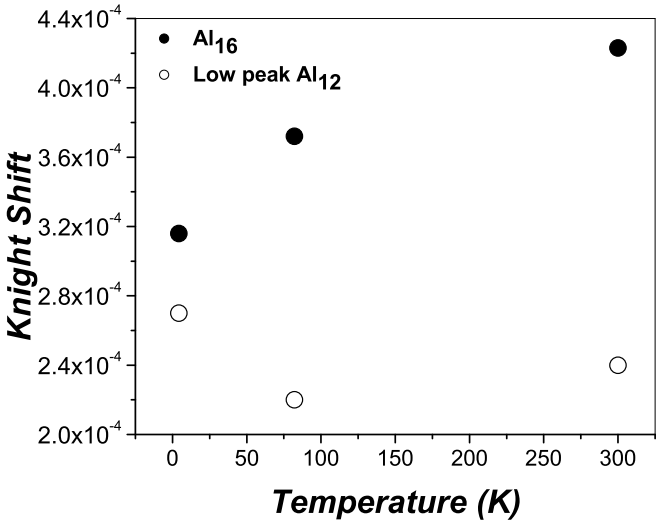

Fig. 34. Temperature dependence of Knight shift for the single peak of $Ba_8Al_{16}Ge_{30}$ and low frequency peak of $Ba_8Al_{12}Ge_{34}$

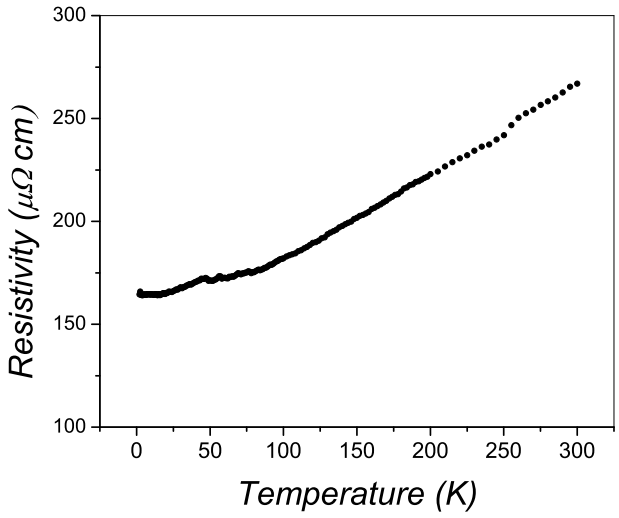

Fig. 35. Temperature dependence of the electrical resistivity of $Ba_8Al_{12}Ge_{34}$ sample

reduced signal/noise ratio at room temperature. Magic angle spinning (MAS) measurements for Al_{12}, shown later, confirmed that the broad quadrupole background still is present at room temperature.

Only considering the first order quadrupole and anisotropic Knight shift effects, the equation describing the experimentally observed NMR transition frequency between the m^{th} and $(m-1)^{th}$ level in a single crystal is given by [34]

$$\begin{aligned} \nu(m \leftrightarrow m-1) &= \nu_0 + [\frac{1}{2}\nu_Q(m-\frac{1}{2}) + \frac{K_1\nu_{ref}}{2}](3\mu^2-1) \\ -\frac{1}{2}[K_2\nu_{ref} &+ (m-\frac{1}{2})\nu_Q\eta](1-\mu^2)cos2\phi, \end{aligned} \tag{5.9}$$

where ν_0 is the frequency of true center of the resonance including the isotropic Knight Shift, K_1 is Knight Shift in axial direction, and K_2 is the difference of Knight Shift between the x and y directions. In Eqn. 5.9, ν_{ref} is the frequency of zero shift for the detected nucleus, η is the asymmetry parameter of the electric field gradient (EFG), ϕ is the azimuthal angle, $\mu = \cos\theta$, and ν_Q is proportional to the EFG in the z direction, given by

$$\nu_Q = \frac{3e^2qQ}{2I(2I-1)h}, \tag{5.10}$$

where Q is nuclear quadrupole moment ($0.150\times10^{-28}(m^2)$ for Al), and I is the nuclear spin ($\frac{5}{2}$ for Al). In Eqn. 5.10, eq is the z-direction EFG and given by

$$eq = \frac{\partial^2 V}{\partial z^2}. \tag{5.11}$$

I simulated the quadrupole lineshape according to Eqn. 5.9 by summing over the contributions from $m = \frac{5}{2}$, $\frac{3}{2}$, -$\frac{1}{2}$, and -$\frac{3}{2}$, and assuming equal weight from each m. The crystal orientation was assumed to be evenly distributed over all solid angles. The best simulation results are shown in Fig. 37. In the calculation, ν_Q and ν_{ref} were

set to be a dimensionless value 1, and later converted to frequency after comparing with the experimental data. Fitted K_1 and K_2 values are small and close to zero, and in the calculation they have little effect on the overall lineshape. The most important effect comes from η. The best result was obtained with $\eta = 0.4$, and for ν_Q around 210 KHz.

The central line ($\frac{1}{2} \leftrightarrow$ -$\frac{1}{2}$) broadening ($\Delta\nu$) due to second order quadrupole effects was calculated using [34]

$$\frac{e^2qQ}{h} = 5.7\sqrt{\nu_0\Delta\nu}, \tag{5.12}$$

where η is assumed to be zero. For $\eta \neq 0$, the values are very similar. This is appropriate for a nuclear spin $\frac{5}{2}$, like the Al nucleus. Calculation shows that $\Delta\nu$ is less than 1 KHz, which is much less than the splitting of two main peaks in $Ba_8Al_{12}Ge_{34}$. The result confirms that two peaks of $Ba_8Al_{12}Ge_{34}$ are not separated by the central line splitting due to second order quadrupole effects. Indeed T_1 measurements indicated them to be from different framework sites, as we have described earlier. The splitting of two main peaks is small enough that we cannot say from the simulation with which peak the quadrupole line is associated. However, magic angle spinning (MAS) measurement confirmed that the quadrupole line is associated with low frequency peak, as shown next.

Magic angle spinning (MAS) measurements on the $Ba_8Al_{12}Ge_{34}$ sample were carried out at room temperature with spinning frequency 11 KHz and 14 KHz. The result is shown in Fig. 38, which is a snapshot of the actual figure, since unfortunately the computer in the chemistry facility could not give raw data files. We observed two main peaks, the same as we obtained from the spin echo experiments, along with a series of spinning sidebands. From the series of peak positions of the spinning sidebands measured at two different spinning frequencies, we identified that the broad

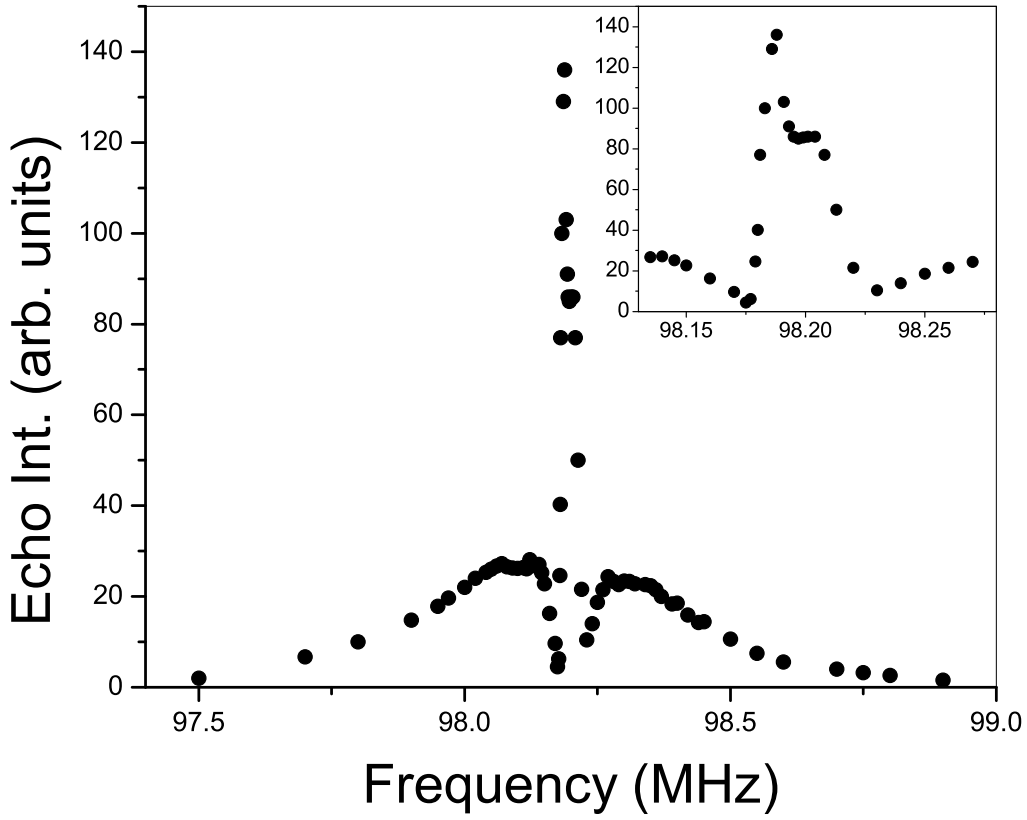

Fig. 36. Lineshapes of $Ba_8Al_{12}Ge_{34}$ at temperature 4.2 K

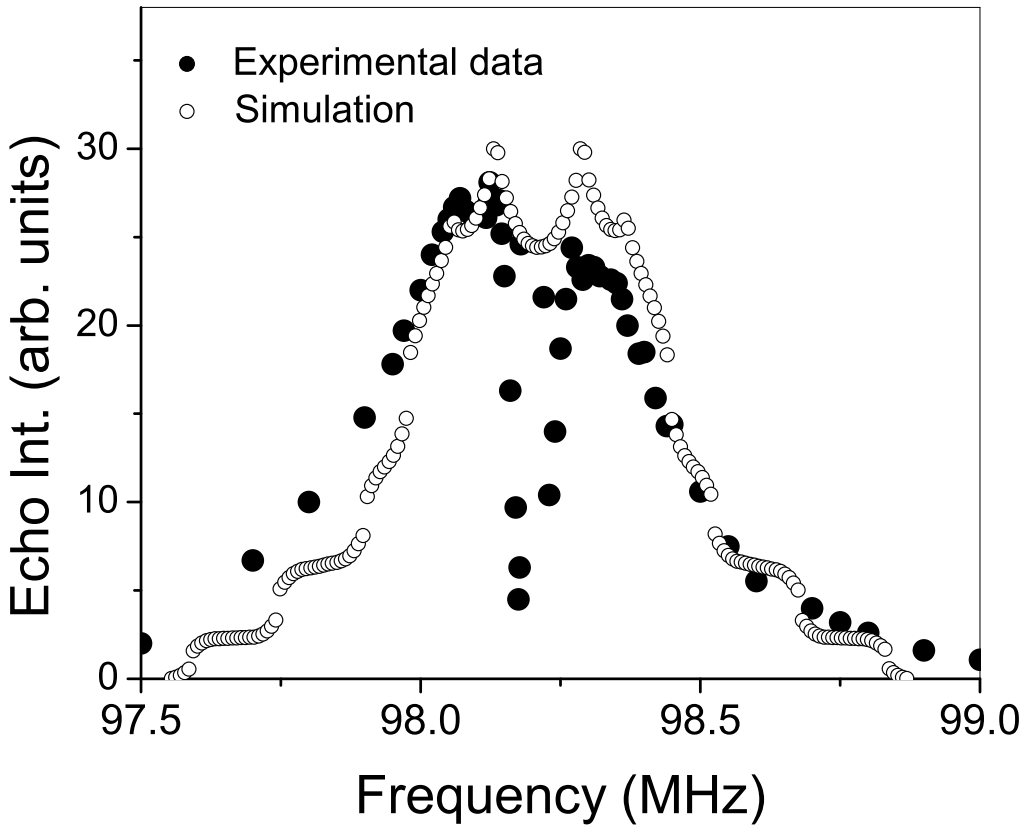

Fig. 37. Simulation of quaduapole contribution to lineshape of $Ba_8Al_{12}Ge_{34}$ at 4.2 K

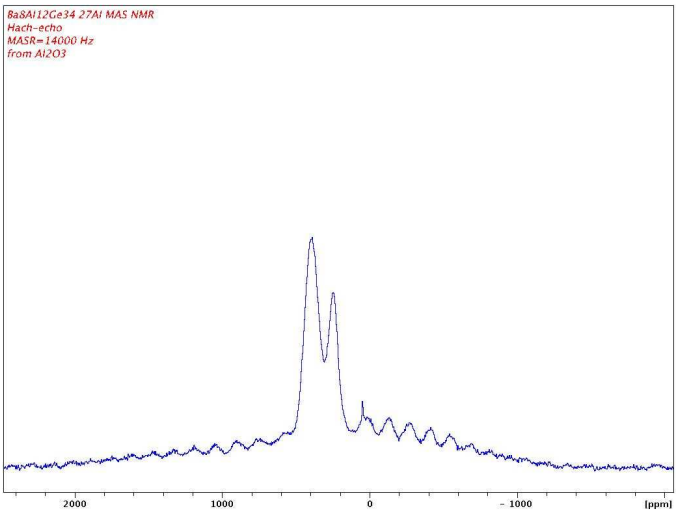

Fig. 38. MAS measurement of $Ba_8Al_{12}Ge_{34}$ at room temperature

quadrupole background is centered at 240 ppm, which is underneath the low frequency peak. The result is shown in Fig. 39. A similar MAS measurements were performed on $Ba_8Al_{16}Ge_{30}$. We observed a single peak for the Al_{16} sample around 300 ppm, along with a series of spinning sidebands like in Al_{12} case. However, the spinning sidebands analysis for Al_{16} sample shows that the broad quadrupole background is centered at 330 ppm, which is a bit higher than the main peak frequency, a result different from Al_{12}. We also did MAS measurements on Al_{13} sample, we observed two main peaks. However, the spinning sidebands for this sample are not so clean as in the Al_{12} sample, so that it is difficult to do analysis on them.

From the various NMR measurements, we have a clear picture of the BaAlGe clathrates. Al_{12} is not just a simple version of Al_{16} with less Al. Rather, the Al deficient samples have a concentration of vacancies similar to that of $Ba_8Ge_{43}[]_3$ [69, 70, 71], apparently resulting in an ordered Al occupation in these samples, with the Al atom more likely to be the neighbor of a vacancy. For Al_{16}, because of the disordered

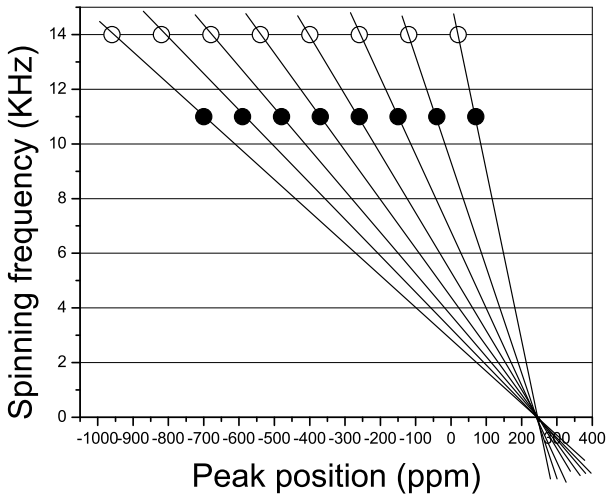

Fig. 39. Fitting of spinning sidebands from MAS measurement of $Ba_8Al_{12}Ge_{34}$ at room temperature

Al occupation of the 3 framework sites, we see a single broad NMR peak due to the inhomogeneous Knight shift of the different sites. For Al_{12}, we clearly see two distinct peaks from two sites, which also indicates that Al occupation in this sample has a degree of ordering. From the various NMR measurements, we know that at least one Al site corresponds to the observed quadrupole background. For Al_{12}, it is clear that the main part of the observed quadrupole background is centered at the low frequency peak which we assigned to Al neighboring the vacancies. For Al_{16}, the quadrupole background is spread out due to the disorder of the Al sites, so that no distinct satellite peaks could be identified.

To further analyze the results, we carried out EFG calculations using the WIEN2k ab initio package. There are three framework sites, and a total of 46 framework positions, and Al can occupy any one of them. Therefore, if we wanted to calculate the EFG for $Ba_8Al_{12}Ge_{34}$ assuming random occupancy, a large supercell structure would

be required, which could be difficult or impossible to calculate. Since we are only interested in the EFG of Al on three framework sites, to simplify the calculation, we assumed that the Al completely occupies each of the three framework sites in turn. We performed EFG calculations for $Ba_8Al_6Ge_{40}$ assuming complete Al occupancy on the $6c$ site, $Ba_8Al_{16}Ge_{30}$ assuming complete Al occupancy on the $16i$ site, and $Ba_8Al_{24}Ge_{22}$ assuming complete Al occupancy on the $24k$ site. Even though the repeating structure contains only one unit cell, there are still a total of 54 atoms in each cell providing a reasonable approximation to the superstructure. It took 3 days to finish one calculation. ν_Q was calculated from Eqn. 5.10 and Eqn. 5.11. The EFG results for each Al site are shown Table III. The results show that η is not equal to zero only when Al is on $24k$ site, with $\nu_Q = 174$ KHz. These values are close to what we have obtained from simulation of quadrupole lines, with $\eta = 0.4$ and $\nu_Q \approx 210$ KHz. Thus it may be that the low-frequency peak is dominated by $24k$ site, although that site also has a vacancy neighbor. Another indication of this is that the vacancies prefer to occupy the $6c$ site [69, 70, 71], for which the only neighbors are the $24k$ site, and the low-frequency peak of Al_{12} is associated with a framework site neighboring with vacancies. This result is different from what had been reported earlier in refrence [74], where it was reported that in $Ba_8Al_{16}Ge_{30}$ the $6c$ and $24k$ sites are occupied completely by Al and Ge, respectively, whereas the $16i$ site is shared by Al and Ge. However, due to the presence of the vacancies, the site occupation will be different, since vacancies would naturally try to draw the Al close to them. To confirm, we plan to calculate the vacancy induced EFG using a supercell approach, now that we have installed the Wien2K package at the supercomputer center. We note in Table III that EFG on $6c$ is not equal to zero, apparently contradictory to the high symmetry of $6c$. This was a surprise for which we do not yet have a physical explanation.

Table III. EFG and ν_Q of Al site of $Ba_8Al_xGe_{40-x}$ with x = 6, 16, and 24 assuming completely Al occupancy of one of $6c$, $16i$, and $24k$ sites. (EFG is in units $10^{21}V/m^2$, and η is dimensionless).

	V_{xx}	V_{yy}	V_{zz}	η	ν_Q (kHz)	Al site
$Ba_8Al_6Ge_{40}$	-0.279	-0.279	0.558	0	304	$6c$
$Ba_8Al_{16}Ge_{30}$	1.021	1.021	-2.04	0	1110	$16i$
$Ba_8Al_{24}Ge_{22}$	-0.278	0.046	0.32	0.75	174	$24k$

3. Summary

Now I would like to briefly summarize the results on $Ba_8Al_xGe_{40-x}$. With x = 12 and 13, we observed two peaks, with one attributed to vacancies, consistent with WDS results. In $Ba_8Al_{16}Ge_{30}$ we observed a single peak, and the broadening of this peak we attribute is due to an inhomogeneous Knight shifts for Al nuclei located on these framework sites. A broad quadrupole background exists for all Al samples. The difference in broadening between Al_{12} and Al_{16} NMR is apparently due to the ordering of Al site occupation in Al_{12}, which is absent for Al_{16} sample.

CHAPTER VI

CONCLUSIONS

I did studies for the clathrates $Ba_8Ga_{16}Sn_{30}$, $Sr_8Ga_{16}Ge_{30}$, $Ba_8Ga_{16}Ge_{30}$, and $Ba_8Al_xGe_{40-x}$ with x = 12, 13 and 16. Among these $Ba_8Ga_{16}Sn_{30}$ is a type-VIII clathrate, while others are type-I clathrates.

Resistivity measurement on $Ba_8Ga_{16}Sn_{30}$ showed it to have semiconductor behavior. Specific heat measurement indicates the existence of Einstein oscillator modes. Fitting of the specific heat data yielded $\gamma = 9$ mJ/(mol K^2), with a Debye temperature $\Theta_D = 187$ K, and Einstein temperature $\Theta_E = 51$ K.

Sr and Ba clathrates exhibit different NMR results. The T_1 of $Sr_8Ga_{16}Ge_{30}$ obeys the Korringa relation, implying normal metallic behavior for the Sr clathrate, as expected for a heavily doped n-type semiconductor. For $Ba_8Ga_{16}Ge_{30}$ sample, the relaxation behavior (T_1) deviates from the Korringa relation, and the Knight shift and linewidth change with temperature. These results could be explained by carrier freezout in the Ba clathrate, and the development of a dilute set of magnetic moments due to these localized carriers. On the other hand, in Sr clathrate, there was no sign of carrier freezout in the system.

For $Sr_8Ga_{16}Ge_{30}$, linewidth changes with temperature is one of the features that indicates slow atomic motion. Fitting the lineshape changes yielded an activation energy of about 7 K. CPMG measurements yielded results that are consistent with the linewidth changes. By a simple model, we obtained an activation energy E_a=4.6 K for Sr hopping, which is similar to the value obtained from linewidth measurements. This model assumed a wide distribution of hopping rates, and an asymmetric well model worked well to explain the data.

NMR studies on $Ba_8Ga_{16}Ge_{30}$ made from Ga flux shows behavior different from

that of samples made with the stoichiometric ratio, which indicates a dramatically different electronic structure in this sample. The p type sample has a smaller Knight shift and a slower relaxation rate than n type samples made with the stoichiometric ratio, which is consistent with a change in orbital symmetry between the conduction and valence bands.

In Al NMR measurements on $Ba_8Al_xGe_{40-x}$ with $x = 12$ and 13, we found that T_1 of all Al samples follows the Korringa relation. The broadening of the single peak of Al_{16} is due to the inhomogeneous Knight shifts for occupation of different framework sites. For Al_{12} and Al_{13}, we observed two peaks, and NMR results show that they are from distinct Al sites, while for each peak, the inhomogeneous broadening is much smaller. The difference in lineshapes we attributed to the existence of vacancies which we detected in the Al-deficient materials, and we assign one of the two Al peaks to Al adjacent to a vacancy. The difference in broadening between Al_{12} and Al_{16} is apparently due to the degree of ordering in Al_{12}. For the Al_{12} sample, simulation of the quadrupole background and WIEN2k calculations indicate that the low-frequency peak is dominated by the $24k$ site, which is also consistent with crystal structure, where $6c$, which vacancies prefer to occupy, only has $24k$ site neighbors.

REFERENCES

[1] E. D. Sloan, *Clathrate Hydrates of Natural Gases,* New York: Marcel Dekker, 1997.

[2] W. L. Mao, H. K. Mao, A. F. Goncharov, V. V. Struzhkin, Q. Guo, J. Hu, J. Shu, R. J. Hemley, M. Somayazulu and Y. Zhao, "Hydrogen clusters in clathrate hydrate," *Science*, vol. 279, pp. 2247 - 2249, 2002.

[3] G. A. Jeffrey, "Hydrate inclusion in: inclusion compounds," in *Structure Aspects of Inclusion Compounds Formed by Inorganic and Organ Metallic Host Lattices*. J. L. Atwood, J. E. D. Davies and D. D. MacNicol, Eds. London: Academic Press, 1984, pp.1 - 100

[4] S. Paschen, W. Carrillo-Cabrera, A. Bentien, V. H. Tran, M. Baenitz, Yu. Grin and F. Steglich, "Structural, transport, magnetic, and thermal properties of $Eu_8Ga_{16}Ge_{30}$," *Phys. Rev. B*, vol. 64, pp. 214404.1 - 11, 2001.

[5] B. C. Sales, B. C. Chakoumakos, R. Jin, J. R. Thompson and D. Mandrus, "Structural, magnetic, thermal and transport properties of $X_8Ga_{16}Ge_{30}$ (X = Eu, Sr, Ba) single crystals," *Phys. Rev. B*, vol. 63, pp. 245113.1 - 8, 2001.

[6] G. S. Nolas, T. J. R. Weakley, J. L. Cohn and R. Sharma, "Structural properties and thermal conductivity of crystalline Ge clathrates," *Phys. Rev. B*, vol. 61, pp. 3845 - 3850, 2000.

[7] G. K. H. Madsen, K. Schwarz, P. Blaha and D. J. Singh, "Electronic structure and transport in type-I and type-VIII clathrates containing strontium, barium and europium," *Phys. Rev. B*, vol. 68, pp. 125212.1 - 7, 2003.

[8] A. Bentien, M. Christensen, J. D. Bryan, A. Sanchez, S. Paschen, F. Steglich, G. D. Stucky and B. B. Iversen, "Thermal conductivity of thermoelectric clathrates," *Phys. Rev. B*, vol. 69, pp. 045107.1 - 5, 2004.

[9] L. Qiu, I. P. Swainson, G. S. Nolas and M. A. White, "Structure, thermal and transport properties of the clathrates $Sr_8Zn_8Ge_{38}$, $Sr_8Ga_{16}Ge_{30}$ and $Ba_8Ga_{16}Si_{30}$," *Phys. Rev. B*, vol. 70, pp. 035208.1 - 8, 2004.

[10] B. C. Chakoumakos, B. C. Sales, D. G. Mandrus and G. S. Nolas, "Structural disorder and thermal conductivity of the semiconducting clathrate $Sr_8Ga_{16}Ge_{30}$," *J. Alloys Compd.*, vol. 296, pp. 80 - 86, 2000.

[11] G. S. Nolas, J. L. Cohn, G. A. Slack and S. B. Schujman, "Semiconducting Ge clathrates: Promising candidates for thermoelectric applications," *Appl. Phys. Lett.*, vol. 73, pp. 178 - 180, 1998.

[12] T. Kawaguchi, K. Tanigaki and M. Yasukawa, "Ferromagnetism in germanium clathrate: $Ba_8Mn_xGe_{46-x}$," *Appl. Phys. Lett.*, vol. 77, pp. 3438 - 3400, 2000.

[13] Y. Li, J. Chi, W. Gou, S. Khandekar and J. H. Ross, Jr., "Structure and stability of BaCuGe type-I clathrates," *J. Phys.: Condens. Matter*, vol. 15, pp. 5535 - 5542, 2003.

[14] S. Srinath, J. Gass, D. J. Rebar, G. T. Woods, H. Srikanth and G. S. Nolas, "Giant magnetocaloric effect in clathrates," *J. Appl. Phys.*, vol. 99, pp. 08K902.1 - 3, 2006.

[15] S. Yamanaka, E. Enishi, H. Fukuoka, and M. Yasukawa, " High-pressure synthesis of a new silicon clathrate superconductor, Ba_8Si_{46}," *Inorg. Chem.*, vol. 39, pp. 56 - 58, 2000.

[16] K. Moriguchi, M. Yonemura and A. Shintani, "Electronic structures of Na_8Si_{46} and Ba_8Si_{46}," *Phys. Rev. B*, vol. 61, pp. 9859 - 9862, 2000.

[17] Y. Li, R. Zhang, Y. Liu, N. Chen, Z. P. Luo, X. Ma, G. Cao, Z. S. Feng, C. R. Hu and J. H. Ross, Jr., "Superconductivity in gallium-substituted Ba_8Si_{46} clathrates," *Phys. Rev. B*, vol. 75, pp. 054513.1 - 8, 2007.

[18] Y. Li, Y. Liu, N. Chen, G. Cao, Z. Feng and J. H. Ross, Jr., "Vacancy and copper-doping effect on superconductivity for clathrate materials," *Phys. Lett. A*, vol. 345, pp. 398-408, 2005.

[19] J. L. Cohn, G. S. Nolas, V. Fessatidis, T. H. Metcalf and G. A. Slack, "Glasslike heat conduction in high-mobility crystalline semiconductors," *Phys. Rev. Lett.*, vol. 82, pp. 779 - 782, 1999.

[20] V. Keppens, B. C. Sales, D. Mandrus, B. C. Chakoumakos and C. Laermants, "When does a crystal conduct heat like glass?" *Philos. Mag. Lett.*, vol. 80, pp. 807 - 812, 2000.

[21] I. Zerec, V. Keppens, M. A. McGuire, D. Mandrus, B. C. Sales and P. Thalmeier, "Four-well tunneling states and elastic response of clathrates," *Phys. Rev. Lett.*, vol. 92, pp. 185502 - 185505, 2004.

[22] K. Suekuni, M. A. Avila, K. Umeo, and T. Takabatake, "Cage-size control of guest vibration and thermal conductivity in $Sr_8Ga_{16}Si_{30-x}Ge_x$," *Phys. Rev. B*, vol. 75, pp. 195210.1 - 6, 2007.

[23] N. L. Okamoto, K. Kishida, K. Tanaka, and H. Inui "Effect of In additions on the thermoelectric properties of the type-I clathrate compound $Ba_8Ga_{16}Ge_{30}$," *J. Appl. Phys.*, vol. 75, pp. 113525.1 - 5, 2007.

[24] K. Umeo, M. A. Avila, T. Sakata, K. Suekuni and T. Takabatake, "Probing glasslike excitations in single-crystalline $Sr_8Ga_{16}Ge_{30}$ by specific heat and thermal conductivity," *J. of Phys. Society of Japan*, vol. 74, pp. 2145 - 2148, 2005.

[25] A. Bentien, S. Johnsen and B. B. Iversen, "Strong phonon charge carrier coupling in thermoelectric clathrates," *Phys. Rev. B*, vol. 73, pp. 094301.1 - 4, 2006.

[26] F. Bridges and L. Downward, "Possible mechanism for glass-like thermal conductivities in crystals with off-center atoms," *Phys. Rev. B*, vol. 70, pp. 140201.1 - 4, 2004.

[27] R. Baumbach, F. Bridges, L. Downward, D. Cao, P. Chesler and B. Sales, "Off-center phonon scattering sites in $Eu_8Ga_{16}Ge_{30}$ and $Sr_8Ga_{16}Ge_{30}$," *Phys. Rev. B*, vol. 71, pp. 024202.1 - 19, 2005.

[28] R. P. Hermann, W. Schweika, O. Leupold, Rudolf R*ü*fer, G. S. Nolas, F. Grandjean and G. J. Long, "Neutron and nuclear inelastic scattering study of the Einstein oscillators in Ba-, Sr-, and Eu-filled germanium clathrates," *Phys. Rev. B*, vol. 72, pp. 174301.1 - 6, 2005.

[29] M. A. Avila, K. Suekuni, K. Umeo, H. Fukuoka, S. Yamanaka and T. Takabatake, "Glasslike versus crystalline thermal conductivity in carrier-tuned $Ba_8Ga_{16}X_{30}$ clathrates (X=Ge, Sn)," *Phys. Rev. B*, vol. 74, pp. 125109.1 - 8, 2006.

[30] A. Saramat, G. Svensson, A. E. C. Palmqvista, C. Stiewe, E. Mueller, D. Platzek, S. G. K. Williams, D. M. Rowe, J. D. Bryan and G. D. Stucky, "Large thermoelectric figure of merit at high temperature in Czochralski-grown clathrate $Ba_8Ga_{16}Ge_{30}$," *J. Appl. Phys.*, vol. 99, pp. 023708.1 - 5, 2006.

[31] J. Gryko, P. F. McMillan, R. F. Marzke, A. P. Dodokin, A. A. Demkov and

O. F. Sankey, "Temperature-dependent ^{23}Na Knight shifts and sharply peaked structure in the electronic densities of states of Na-Si clathrates," *Phys. Rev. B*, vol. 57, pp. 4172 - 4179, 1998.

[32] C. P. Slichter, *Principles of Magnetic Resonance,* New York: Springer-Verlag, 1990.

[33] A. Abragam, *Principles of Nuclear Magnetism,* London: Oxford University Press, 1982.

[34] G. C. Carter, L. H. Bennett and D. J. Kahan, *Metallic Shifts in NMR,* Oxford: Pergamon, 1977.

[35] H. Alloul and P. Dellouve, "Spin localization in Si:P-direct evidence from ^{31}P NMR," *Phys. Rev. Lett.*, vol. 59, pp. 578 - 581, 1987.

[36] B. Sriram Shastry and E. Abrahams, "What does the Korringa ratio measure?" *Phys. Rev. Lett.*, vol. 72, pp. 1933 - 1936, 1994.

[37] David Pines, "A collective description of electron interactions: IV. electron interaction in metals," *Phys. Rev.*, vol. 92, pp. 626 - 636, 1953.

[38] T$\hat{o}$ru Moriya, "The effect of the electron-electron interaction on the nuclear spin relaxation in metals," *J. Phys. Soc. Jpn.*, vol. 18, pp. 516 - 520, 1963.

[39] Dieter Wolf, *Spin-Temperature and Nuclear-spin Relaxation in Matter*, Clarendon: Oxford, 1979.

[40] A. Narath, "Nuclear spin-lattice relaxation in hexagonal transition metals: Titanium," *Phys. Rev.*, vol. 162, pp. 320 - 332, 1967.

[41] C. S. Lue and J. H. Ross, Jr., "Semimetallic behavior in Fe_2VAl: NMR evidence," *Phys. Rev. B*, vol. 58, pp. 9763 - 9766, 1998.

[42] Neil W. Ashcroft and N. David Mermin *Solid State Physics,* Orlando: Harcourt, 1976.

[43] D. Huo, T. Sakata, T. Sasakawa, M. A. Avila, M. Tsubota, F. Iga, H. Fukuoka, S. Yamanaka, S. Aoyagi, and T. Takabatake, "Structural, transport, and thermal properties of the single-crystalline type-VIII clathrate $Ba_8Ga_{16}Sn_{30}$," *Phys. Rev. B*, vol. 71, pp. 075113.1 - 6, 2005.

[44] Y. Zhang, P. L. Lee, G. S. Nolas and A. P. Wilkinson, "Gallium distribution in the clathrates $Sr_8Ga_{16}Ge_{30}$ and $Sr_4Eu_4Ga_{16}Ge_{30}$ by resonant diffraction," *Appl. Phys. Lett.*, vol. 80, pp. 2931 - 2933, 2002.

[45] O. Kanert and M. Mehring, "Static quadrupole effects in disordered cubic solids," in *NMR: Basic Principles and Progress.* E. Fluck and R. Kosfeld, Eds. New York: Springer-Verlag, 1971, pp. 1 - 81.

[46] F. Shimizu, Y. Maniwa, K. Kume, H. Kawaji, S. Y. and M. Ishikawa, " NMR study in the superconducting silicon clathrate compound $Na_xBa_ySi_{46}$," *Phys. Rev. B*, vol. 54, pp. 13242 - 13246, 1996.

[47] V. L. Kuznetsov, L. A. Kuznetsova, A. E. Kaliazin and D. M. Rowe, "Preparation, thermoelectric properties of $A_8^{II}B_{16}^{III}B_{30}^{IV}$ clathrate compounds," *J. Appl. Phys.*, vol. 11, pp. 7871 - 7875, 2000.

[48] S. E. Latturner, J. D. Bryan, N. Blake, H. Metiu and G. D. Stucky, "Siting of antimony dopants and Galllium in $Ba_8Ga_{16}Ge_{30}$ clathrates grown from Gallium flux," *Inorg. Chem.*, vol. 41, pp. 3956 - 3961, 2002.

[49] B. J. Suh, F. Borsa and D. R. Torgeson, "Use of an alternating-phase CPMG sequence to avoid spin-locking effects in T_2 measurements in solids," *J. Magn. Reson. A*, vol. 110, pp. 58 - 61, 1994.

[50] R. L. Vold, R. R. Vold and H. E. Simon, "Errors in measurements of transverse relaxation rates," *J. Magn. Reson.*, vol. 11, pp. 283 - 298, 1973.

[51] G. S. Nolas and C. A. Kendziora, "Raman scattering study of Ge, Sn compounds with type-I clathrate hydrate crystal structure," *Phys. Rev. B*, vol. 62, pp. 7157 - 7161, 2000.

[52] D. L. Cox and A. Zawadowski, "Exotic Kondo effects in metals: Magnetic ions in a crystalline electric field and tunnelling centres," *Adv. Phys.*, vol. 47, pp. 599 - 942, 1998.

[53] Pablo Esquinazi, *Tunneling Systems in Amorphous and Crystalline Solids*, Berlin: Springer-Verlag, 1998.

[54] A. Halbritter, L. Borda, A. Zawadowski, "Slow two-level systems in point contacts," *Adv. Phys.*, vol. 53, pp. 939 - 1010, 2004.

[55] F. Tournus, B. Masenelli, P. Mélinon, D. Connétable, X. Blase, A. M. Flank, P. Lagarde, C. Cros and M. Pouchard, "Guest displacement in silicon clathrates," *Phys. Rev. B*, vol. 69, pp. 035208.1 - 6, 2004.

[56] B. H. Toby, "EXPGUI, a graphical user interface for GSAS," *J. Appl. Cryst.*, vol. 34, pp. 210 - 213, 2001.

[57] A. C. Larson and R. B. von Dreele, "General structure analysis system (GSAS)," LAUR 86-748, Los Alamos National Laboratory, 2000.

[58] Y. Li, W. Gou, J. Chi, V. Goruganti and J. H. Ross, Jr., "Transition-metal substitution in semiconducting $Ba_8Ga_{16}Ge_{30}$ clathrates," *AIP Conf. Proc.*, vol. 772, pp. 331 - 332, 2005.

[59] M. P. Marder, *Condensed Matter Physics,* New York: Wiley-Interscience, 2000.

[60] N. L. Okamoto, K. Kishida, K. Tanaka, and H. Inui, "Crystal structure and thermoelectric properties of type-I clathrate compounds in the BaGaGe system," *Appl. Phys. Lett.*, vol. 100, pp. 073504.1 - 10, 2006.

[61] J. Blatt, *Thermoelectric Power of Metals,* New York: Springer-Verlag, 1976.

[62] N. P. Blake, S. Latturner, J. D. Bryan, Galen D. Stucky and H. Metiu, "Band structures and thermoelectric properties of the $Ba_8Ga_{16}Ge_{30}$, $Sr_8Ga_{16}Ge_{30}$, $Ba_8Ga_{16}Si_{30}$ and $Ba_8In_{16}Sn_{30}$," *J. Chem. Phys.* , vol. 115, pp. 8060-8073, 2001.

[63] W. Götze and W. Ketterle, " Nuclear spin relaxation in disordered conductors," *Z. Phys. B*, vol.54, pp. 49-57, 1983

[64] G. A. Thomas, "Critical exponent of the metal-insulator transition," *Phil. Mag. B.*, vol. 52, pp. 479 -498, 1983.

[65] M. J. R. Hoch and D. F. Holcomb, "^{31}P Knight shifts and spin dynamics in Si:P at temperatures comparable to the Fermi temperature," *Phys. Rev. B*, vol. 71, pp. 035115.1 - 6, 2005.

[66] E. M. Meintjes, J. Danielson and W. W. Warren, Jr., "Temperature-dependent NMR study of the impurity state in heavily doped Si:P," *Phys. Rev. B*, vol. 71, pp. 035114.1 - 14, 2005.

[67] W. Gou, Y. Li, J. Chi, J. H. Ross, Jr., M. Beekman and G. S. Nolas, "NMR study of slow atomic motion in $Sr_8Ga_{16}Ge_{30}$ clathrate," *Phys. Rev. B*, vol. 71, pp. 174307.1 - 6, 2005.

[68] D. Paget, G. Lampel and B. Sapoval, "Low field electron-nuclear spin coupling in gallium arsenide under optical pumping conditions," *Phys. Rev. B*, vol. 15, pp. 5780 - 5796, 1977.

[69] H. Fukuoka, J. Kiyoto, S. Yamanaka, "Superconductivity and crystal structure of the solid solutions of $Ba_{8-\delta}Si_{46-x}Ge_x$ ($0 \leq x \leq 23$) with Type I clathrate structure," *J. Solid State Chem.*, vol. 175, pp. 237 - 244, 2003.

[70] W. Carrillo-Cabrera, S. Budnyk, Y. Prots, and Y. Grin, "Ba_8Ge_{43} revisited: a $2a' \times 2a' \times 2a'$ superstructure of the clathrate-I type with full vacancy ordering," *Anorg. Allg. Chem.*, vol. 630, pp. 2267 - 2276, 2004.

[71] H. Shimizua, T. Iitaka, T. Fukushima, T. Kume, S. Sasaki, N. Sata, Y. Ohishi, H. Fukuoka and S. Yamanaka, "Raman and x-ray diffraction studies of Ba doped germanium clathrate Ba_8Ge_{43} at high pressures," *J. Appl. Phys.*, vol. 101, pp. 063549.1 - 7, 2007.

[72] Y. Li, *et al.*, "Private communications", 2005

[73] C. L. Condron, J. Martin, G. S. Nolas, P. M. B. Piccoli, A. J. Schultz and S. M. Kauzlarich, "Structure and thermoelectric characterization of $Ba_8Al_{14}Si_{31}$," *Inorg. Chem.*, vol. 45, pp. 9381 - 9386, 2006.

[74] B. Eisenmann, H. Schäfer and R. Zagler, "die verbindungen $A_8^{II}B_{16}^{III}B_{30}^{IV}$ (A^{II} = Sr,Ba; B^{III} = Al, Ga; B^{IV} = Si, Ge, Sn) und ihre kafigstruk-turen," *J. Less-Common Met.*, vol. 118, pp. 43 - 45, 1986.

VITA

Weiping Gou

Department of Physics

c/o Dr. Joseph Ross

Texas A&M University

College Station, TX 77843-4242

Weiping Gou was born in Xingjiang, China. He received his B.S. degree in physics from Lanzhou University, China in 1996. He got his M.S. degree in Nuclear Engineering from the Institute of High Energy Physics, the Academy of Science of China in 2001. He received his M.S. degree in physics from Texas A&M University in 2003, and received his Ph.D. degree in physics from Texas A&M University in 2008. His email address is gouwp@yahoo.com

The typist for this dissertation was Weiping Gou.